

Particle Physics in the LHC Era

G. Barr, R. Devenish, R. Walczak, T. Weidberg

January 7, 2015

Particle Detectors

4

4.1 Introduction

All the experimental discoveries that underpin our understanding of particle physics rely on particle detectors, so that a good knowledge of how these sophisticated devices work is essential. The complexity of particle detectors has grown enormously from very simple beginnings to the very powerful detector systems used at the LHC. As in the rest of this book, we will not take a historical approach but try to find the easiest and most direct way to explain the fundamental physics. We will start in section 4.2 with an overview of a collider detector, focusing on what the requirements are and giving a simple description of how the different sub-systems are used to identify some types of particles and measure the energy of individual particles or ‘jets’. This will give us a good idea of what a collider detector looks like but will tell us nothing about how any particular detector actually works. In order to gain any useful understanding, we need to consider the basic detector physics which will explain quantitatively the performance of real detectors.

We will start this systematic approach in section 4.3 by considering how high energy particles interact with matter and lose energy. The processes result in a relatively small number of electron/ion pairs, so the next issue to¹ consider is how we can use this effect to create a measurable signal. The fundamental detector physics of how signals are generated will be described in section 4.4 as this step is obviously essential for any real understanding of how a particle detector works.

Armed with this knowledge we can start to consider how basic particle detectors actually work. In section 4.6 we will look at two techniques used for tracking the trajectory of charged particles, wire chambers and silicon detectors. Next in section 4.7 we will consider how to make energy measurements for charged and neutral particles in devices called calorimeters.

In order to select interesting events for permanent storage, while rejecting very high rates of background processes, very powerful trigger systems are required. We will review these briefly in section 4.10, with a particular emphasis on LHC collider detectors as these present the largest challenges from the triggering perspective. Even with very powerful trigger systems, many petabytes of data are written to permanent storage every year at the LHC. Therefore extremely powerful computer systems are required to process this data and to run the Monte Carlo simulation programmes used to understand the detector performance and

4.1 Introduction	69
4.2 Overview of Collider Detectors	70
4.3 Particle interactions with matter	72
4.4 Signal generation	79
4.5 Photon Detection	82
4.6 Detectors for charged particle tracks	83
4.7 Detectors for particle jets	95
4.8 Detectors for particle identification	101
4.9 Magnetic fields	103
4.10 Trigger	104
4.11 Detector systems	105
Chapter summary	108
Further reading	108
Exercises	109

¹This is not strictly correct in silicon detectors, where we deal with electron/hole pairs.

²The biggest practical problem with very large computer farms is how to provide sufficient cooling to remove the heat.

correct for the inevitable imperfections. This computing requires 10^5 CPUs, which would be difficult to deal with in one facility². The problem has been solved by the use of ‘Grid’ computing, in which the CPUs are distributed over many computer centres across the world. Grid computing is now a major research area in its own right but will not be covered further in this book.

Having understood the basic building blocks, we then look in section 4.11 at how large particle detectors are designed and work. Here and in other chapters we will use case studies of real detectors to see how the fundamental principles are applied in practice. Interestingly we will see that there is no perfect solution to the many design challenges, and there are always difficult trade-offs in the design of any large detector. The discussion will focus on the design of the general purpose LHC detectors as these are the largest and most sophisticated detector systems ever built. We will also briefly consider neutrino detectors, as the constraints are not the same as for collider detectors and the resulting systems are very different.

4.2 Overview of Collider Detectors

As an example of a Collider detector we will look at the general purpose detectors at the LHC. As will be discussed in chapter 13 the principle aims of the LHC are the study of the Higgs sector and the search for new physics beyond the Standard Model (SM) such as Supersymmetry. Higgs bosons or any exotic particles will be heavy and will in general decay rapidly to SM particles, therefore we need to optimize the detector to energetic SM particles. We therefore wish to measure the momenta of photons, electrons, muons, taus and hadron jets. As well as measuring the momenta, we need to distinguish these different particles, which is non-trivial as the rates for hadron jets are $O(10^6)$ times higher than for leptons. We also need to distinguish jets from b and c quarks from jets from light quarks. For neutrinos or exotic weakly interacting particles, e.g. SUSY WIMPs (see chapter ??) direct detection is clearly impractical. However we can infer the transverse momentum of these ‘invisible’ particles by using conservation of momentum. For this technique to be effective we require detectors with calorimeters that cover most of the 4π solid angle (this technique is discussed in chapter 13).

A very schematic view of the principle components of a general purpose collider detector is shown in fig. 4.2. Working our way out from the centre of the detector we can see how the different elements contribute to satisfying these requirements.

- **Tracker.** This consists of very high precision silicon detectors, immersed in a large magnetic field from a superconducting magnet. The trajectories of charged particles can be reconstructed and hence the momenta can be computed. These are used in conjunction with the calorimeters and muon detector to identify and measure the momenta of electrons, muons and taus. They can also

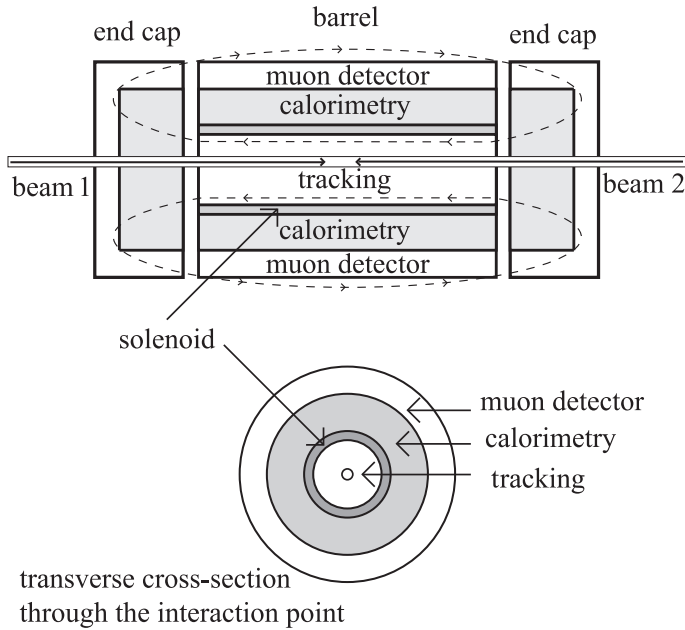


Fig. 4.1: Longitudinal and transverse views of a generic collider detector.

measure the momenta of charged hadrons. The very high precision of the detectors allows good momentum resolution for very high momentum particles. It also allows b and c quarks to be identified, using the fact that the trajectories of their decay products do not point back to the primary vertex because of their relatively long lifetime. Magnetic fields in the range 2 to 4T are created by superconducting magnets³.

- Calorimeter.** The first aim of the calorimeters is to provide high precision measurements of photons and electrons. The second aim is to measure the energy of hadrons and so reconstruct hadronic jets. All particles apart from muons and weakly interacting particles like neutrinos will deposit nearly all their energy in the calorimeters. In general the energies are reconstructed from active detector elements interleaved with passive absorber material. For practical reasons which we will consider in section 4.7, the calorimeters are divided into electromagnetic (EM) and hadronic sections. The calorimeters are divided into small cells which allows for reconstruction of the transverse and longitudinal profiles of the energy deposition. This provides very powerful separation between electrons which deposit nearly all their energy in a small region of the EM calorimeter and hadronic jets which produce deeper and wider showers. In order to reconstruct the missing transverse momentum, it is essential that the calorimeter covers a solid angle as

³The superconducting magnets are based on similar technology to that used for the accelerator (see chapter 3).

⁴Two holes around the beam pipe are unavoidable, so there can be significant energy ‘lost’ down the beam pipes, but as the angles are very small, the transverse momenta are low, hence we can measure missing transverse momentum but not missing longitudinal momentum.

near to 4π as possible⁴.

- **Muon Spectrometer.** If the calorimeter is sufficiently thick, the main particles emerging from the calorimeters will be muons because they do not tend to make electromagnetic showers like electrons, or have hadronic interactions. The trajectories of the muons are measured in large wire chambers and can be matched to high transverse momentum charged particles measured in the tracker, reducing the effects of hadrons ‘leaking’ out of the back of the calorimeter. If there is a magnetic field in the region of the muon chambers, the trajectory of the muon can be used to determine the muon momenta. Possible magnetic field configurations are considered in section 4.9. The momenta of the muons can be measured independently in the tracker and combined with the measurement in the muon spectrometer to get the best precision.

4.3 Particle interactions with matter

In this section we will examine the most important interactions of high energy particles with matter that we need to understand detector physics. For tracking detectors the most important processes is ionization as this generates the electron-ion pairs that we can detect. Multiple scattering is also important in tracking detectors because it limits the resolution. Electromagnetic processes such as pair-production are fundamental for understanding electromagnetic and hadronic calorimeters. Finally hadronic interactions are obviously of particular importance for understanding hadronic calorimeters⁵.

⁵This is of course a very simplified picture, in reality all these processes affect all detector types to some extent.

4.3.1 Ionization

All charged particles interact with electrons in the atoms in any material in the detector. For high energy particles⁶, the energy transferred to the electrons can be larger than the ionization energy, so this will create free electrons and positive ions. These secondary charged particles can be detected as discussed in this chapter. These collisions result in the incident particle losing energy in the lab frame (they are approximately elastic collisions in the CMS)⁷. We can understand the main features of the energy loss by ionization by starting from the formula for Rutherford scattering. The differential cross section (see exercise 4.1) as a function of the 4-momentum transfer (Q^2) and speed of the incoming particle β is given by

$$\frac{d\sigma}{dQ^2} = 4\pi \left(\frac{z\alpha^2}{(\beta Q^2)^2} \right) \quad (4.1)$$

where z is the charge in units of electron charge of the particle scattering with an electron and α is the fine structure constant. We can evaluate Q^2 in the rest frame of the electron before the collision to be (see exercise 4.2) $Q^2 = 2m_e T$ where T is the kinetic energy of the scattered

⁶Here we are typically interested in particles with energies $E \gg 1 \text{ MeV}$

⁷Charged particles can also lose energy by interacting with the atomic nuclei, but the energy transferred by the elastic scattering considered in this section is negligible compared to interactions with electrons because of the larger mass of the nuclei compared to electrons. Electrons also lose energy by bremsstrahlung and this will be discussed in sec 4.3.3

electron. Then using a change of variables in eqn 4.1

$$\frac{d\sigma}{dT} = \frac{2\pi z^2 \alpha^2}{m_e \beta^2 T^2}. \quad (4.2)$$

We can convert this expression for the energy loss in one collision to the average energy loss as a charged particle interacts with many atoms in some medium. The rate of energy loss per length in a medium with N atoms per unit volume and atomic number Z is

$$\frac{dE}{dx} = NZ \int_{T_{min}}^{T_{max}} T \frac{d\sigma}{dT} dT. \quad (4.3)$$

The minimum energy T_{min} is related to the ionization energy I . We can calculate the maximum kinetic energy of the electron in the lab frame by considering a collision in the rest frame in which the direction of motion of the electron is reversed (see exercise 4.2) which gives $T_{max} = 2\beta^2\gamma^2 m_e$. Substituting into eqn 4.3 gives an approximate formula for the rate of energy loss of charged particles

$$\frac{dE}{dx} = \frac{2\pi NZ z^2 \alpha^2}{m_e \beta^2} \ln\left(\frac{2\gamma^2 \beta^2 m_e}{I}\right). \quad (4.4)$$

This shows that the energy loss initially decreases with increasing energy and then rises logarithmically with energy. This formula is modified by relativistic effects to give the Bethe-Bloch formula

$$\frac{dE}{dx} = K \frac{Z}{A\beta^2} \left[\ln \frac{2m_e \beta^2 \gamma^2}{I} - \beta^2 - \frac{\delta(\beta\gamma)}{2} \right] \quad (4.5)$$

where $K = 4\pi N_A r_e^2 m_e$ (N_A is Avogadro's number and r_e is the classical radius of the electron), Z and A are the atomic number and atomic mass number of the nucleus. It is conventional to express the stopping power in units of $\text{MeVg}^{-1}\text{cm}^{-2}$. To transform this to the stopping power per unit length we simply multiply by the density ρ . At relativistic energies the electric field from the primary charged particle flattens and so allows collisions with more distant atoms. However at very high energy this effect is reduced by the polarization of the medium which leads to the 'density effect' correction term, $\delta(\beta\gamma)$. The mean energy loss for charged particle in different media as a function of $\beta\gamma$ are shown in fig ???. The important features of the stopping power are very similar for all targets; at low momentum the stopping power decreases rapidly as the momentum of the incident particle increases and then rises logarithmically at higher momentum. There is a broad minimum around $\beta\gamma \sim 3$ and the value of the minimum is typically in the range 1 to 3 $\text{MeVg}^{-1}\text{cm}^{-2}$. Note that the energy loss by ionization scales with Z of the material, which is very different to the Z^2 scaling that we find for pair-production and bremsstrahlung processes. We have discussed the mean energy loss but there can be very large fluctuations because of the large range of energies that can be lost in a single collision. The spread in the actual energy lost is given by the very broad 'Landau' distribution. Very large 'tails' in the distribution are caused by the emission of single relatively energetic electrons (called ' δ -rays').

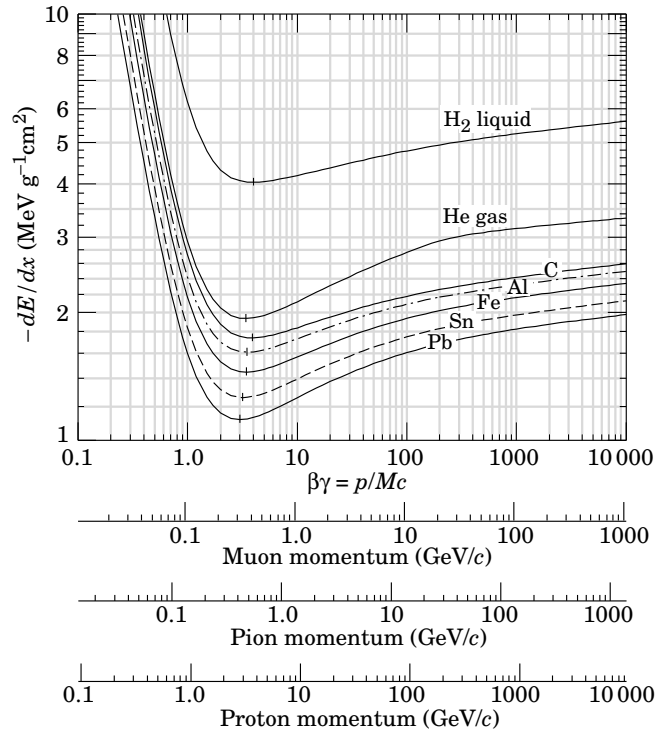


Fig. 4.2: The mean energy loss by ionization in different materials as a function of the $\beta\gamma$ (where β and γ are the usual relativistic factors). Note the units of $\text{MeV g}^{-1}\text{cm}^{-2}$. If one wants to convert to linear stopping power, one needs to multiply by the density.

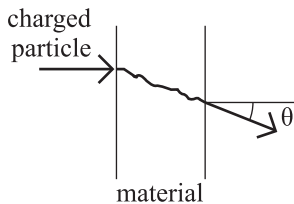


Fig. 4.3 A charged particle undergoing multiple scattering in a material is deflected by an angle θ .

⁸Here the effect of scattering off the atomic nucleus dominates over that from atomic electrons because of the larger charge in the nucleus.

4.3.2 Multiple scattering

When a charged particle traverses a slab of a material, as sketched in fig. 4.3, it undergoes a very large number of very small angle Coulomb scattering with the nuclei⁸. The net result of that is that the particle emerges from the slab at an angle θ with respect to the initial direction. Considering many identical particles, one gets a distribution of their angles θ (in a plane like the plane of fig. 4.3, or for any plane containing the initial direction vector) which follows a Gaussian distribution with the standard deviation

$$\theta_0 = \frac{13.6\text{MeV}}{\beta p} q \frac{x}{X_0} \left(1 + 0.038 \ln \frac{x}{X_0}\right) \quad (4.6)$$

where X_0 is the radiation length, see section 4.3.3, x is the thickness of the material slab, p the momentum, β the velocity and q the charge of the particle. The RMS of the displacement of the particle trajectory y is then $y_{plane}^{rms} = \frac{x}{\sqrt{3}}\theta_0$. The effects of multiple scattering degrade the resolution of track reconstruction and therefore can have profound effects on the detector performance as will be discussed later in this chapter. Note that the amount of multiple scattering scales with the amount of material expressed in radiation lengths so that this provides one motivation for the design tracking detectors which are ‘thin’ in units of radiation lengths. As the radiation length scales with Z^{-2} this shows

that we should minimize the use of high-Z material.

4.3.3 Electromagnetic interactions

Electrons and positrons lose energy by ionization in a similar way to that discussed in section 4.3⁹. However at high energy, the dominant process for energy loss is due to bremsstrahlung (see fig. 4.4). The rate of change of energy for an electron with energy E by bremsstrahlung¹⁰ as a function of distance x is given by

$$\frac{dE}{dx} = -\frac{E}{X_0}. \tag{4.7}$$

where X_0 is the radiation length for the material. We can easily integrate eqn 4.7 to show that in traveling a distance X_0 the electron energy decreases by a factor of $1/e$. An approximate formula for the radiation length is given by (see [?] for the full expression)

$$\frac{1}{X_0} \sim \frac{4\alpha^3 N_A}{m_e^2 A} Z^2 L_{rad} \tag{4.8}$$

where for $Z > 4$, $L_{rad} = \ln(184.15Z^{1/3})$. We can see that the radiation length scales as $1/\alpha^3$ as expected because the Feynman diagram contains three vertices. The electron ‘sees’ the charge of the entire nucleus at one vertex, so the cross section scales¹¹ with the atomic number as $\sim Z^2$. The differential cross section for bremsstrahlung as function of the variable $y = k/E$ where $k(E)$ is the photon (electron) energy is to a good approximation given by

$$\frac{d\sigma}{dk} = \frac{A}{X_0 N_A k} \left(\frac{4}{3} - \frac{4}{3}y + y^2 \right). \tag{4.9}$$

The characteristic feature of eqn 4.9 is that the photon energy spectrum is peaked at low values¹².

High energy photons can undergo pair conversion (see fig. 4.5) which is clearly a closely related process to bremsstrahlung. At high energies, the differential cross section for pair production as a function of the fraction of the photon energy given to the electron, x , is

$$\frac{d\sigma}{dx} = \frac{A}{X_0 N_A} \left(1 - \frac{4}{3}x(1-x) \right). \tag{4.10}$$

We can integrate eqn 4.10 to obtain the total pair production cross section¹³

$$\sigma = \frac{7}{9} \frac{A}{X_0 N_A}. \tag{4.11}$$

At lower energies the dominant process for energy loss by photons, is Compton scattering $\gamma e \rightarrow \gamma e$. Here the incident electron is approximately at rest in an atom and it is ejected from the atom in the process (i.e. in the lab frame energy is transferred from the incident photon to the outgoing electron).

⁹There are some difference however associated with issues like the spin and identical particles for the case of electrons.

¹⁰There are some difference however associated with issues like the spin and identical particles for the case of electrons.

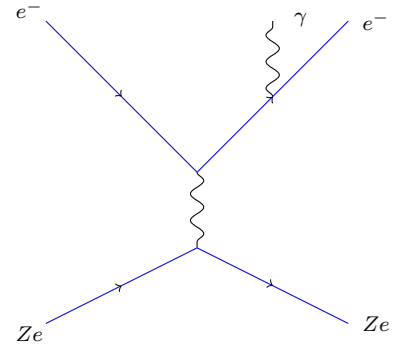


Fig. 4.4 One lowest order Feynman diagram for the bremsstrahlung process $eZ \rightarrow eZ\gamma$, for an electron interacting with a nucleus of charge Ze .

¹¹This scaling with Z is more rapid than the linear scaling with Z we found for energy loss by ionization.

¹²In one radiation length it is very unlikely that the electron will lose energy to only one high energy photon, it is far more common for it to lose energy to many lower energy photons.

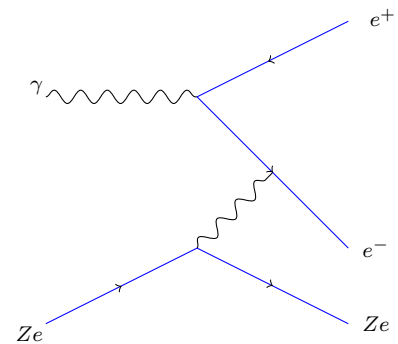
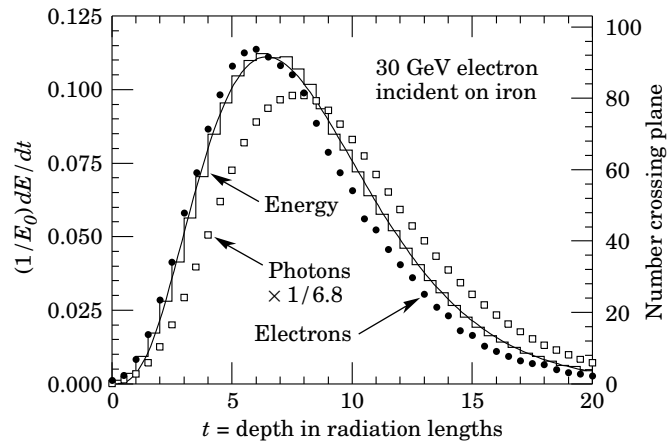


Fig. 4.5 One lowest order Feynman diagram for the pair production process for a photon interacting with a nucleus of charge Ze .

¹³We can see that the length for a primary electron to decrease in energy by a factor f , is a factor of $7/9$ smaller than the length for which the probability of a photon to not make pair production is equal to the same factor f .

Fig. 4.6: Simulation of the longitudinal shower profile for incident 30 GeV electrons on iron. The histogram shows the energy deposition and the circles (squares) indicate the number of electrons (photons). The photons penetrate more deeply than electrons, reflecting the factor of 7/9 in eqn 4.10.



Now that we have considered the fundamental electromagnetic interactions in matter we can understand the nature of the resulting electromagnetic showers. Incident high energy electrons will lose energy by bremsstrahlung and the resulting photons will create e^+e^- pairs which in turn will create more photons by bremsstrahlung. We need to consider the competition between the rate of energy loss from bremsstrahlung/pair production and ionization. The former increases approximately linearly with energy, whereas ionization only increases logarithmically. When the energy of the electrons decreases to the ‘critical energy’ E_c , the energy loss by bremsstrahlung will be equal to that by ionization. An approximate fit to the critical energy as a function of atomic number, Z is given by

$$E_C = \frac{610}{Z + 1.24} \text{MeV}. \quad (4.12)$$

As the electron (positron) energies become lower than E_C , they will lose energy rapidly and become non-relativistic and lose energy by ionization even more rapidly, hence ending the shower development. This results in the shower depth varying logarithmically with energy (see problem ??). The longitudinal shower profile can be calculated rather accurately using Monte Carlo simulations and an example is shown in fig ???. We require nearly complete shower containment to obtain good energy resolution, so we can see that for 30 GeV electrons we need a depth of at least $\sim 20X_0$ ¹⁴. Electromagnetic showers broaden as they penetrate deeper into matter due to multiple coulomb scattering of the electrons (positrons) and the scattering angles involved in bremsstrahlung and pair production. The first effect dominates and we can parameterize the width of the shower by the ‘Moliere radius’, $R_M = X_0 E_s / E_C$ with $E_s \approx 21 \text{MeV}$. Approximately 90% of the energy is contained within a radius of R_M ¹⁵.

¹⁴We can make an average correction to allow for shower leakage out of the back of the calorimeter, but there will always be shower to shower statistical fluctuations in the amount of leakage, which we cannot correct for. Therefore if we want a high resolution electromagnetic calorimeter we must ensure it is deep enough for almost complete shower containment.

¹⁵This sets the natural size for the transverse granularity for electromagnetic calorimeters. We wish to separate electrons (positrons) from hadrons using amongst other measures the transverse shower size. This improves with finer granularity but we clearly do not gain by having cells with lateral dimensions much less than R_M .

4.3.4 Čerenkov radiation

When a charged particle moves at a speed v greater than the local phase velocity of light, $1/n$, where n is the refractive index of the medium, it will emit Čerenkov photons. The angle of the Čerenkov photons relative to the charged particle can be calculated from simple arguments (see fig 4.7). In time t the relativistic particle travels from A to B, a distance of vt . The electromagnetic wave emitted by the particle from A is travelling at a (lower) speed of $1/n$. The wavefront is defined by the plane with a constant phase, is given by the line from C to B. Therefore the Čerenkov angle is given by $\cos \theta_c = 1/(nv)$ ¹⁶. The photons are typically in the optical range and can be detected in a similar way to that used for scintillation light (see section 4.4.2).

4.3.5 Transition radiation

If a high energy charged particle crosses a boundary between two media with different dielectric constants it can emit transition radiation photons. The yield depends on the Lorentz factor γ and therefore allows for the separation of electrons from charged hadrons. The yield per interface is $O(\alpha)$ and is therefore very low, implying that a practical transition radiation detector requires hundreds of interfaces, which can be achieved for example with mylar foils.

4.3.6 Hadronic interactions

High energy hadrons undergo nuclear interactions in matter. The physics involved can not be calculated from first principles and phenomenological models are needed. It is useful to define the interaction length (λ_I) as the length in a material in which the probability of a hadron not-interacting is $1/e$. The cross section at high energy for scattering of a hadron on a nucleus, scales like $\sigma = R_0 A^{2/3}$, which is quite different to the Z^2 scaling for bremsstrahlung and pair-production¹⁷. The interaction length is compared to the radiation length for a few common absorbers used in calorimeters in Table 4.1. The longitudinal shower profile for high energy pions in iron [?] is shown in fig 4.8. We can see that for good shower containment, we need a depth of about $10\lambda_I$, which results in very large calorimeters. This obviously increases the cost of the hadronic calorimeter itself but also increases the radius for the start of the muon detectors, and thus increases the area and cost for the muon spectrometer. Therefore for cost reasons there will usually be some significant energy leakage out of the back of a hadronic calorimeter. As for the case of electromagnetic calorimeters we can make an average correction for this effect but the statistical fluctuations will degrade the resolution.

A high energy hadron interacting with a nucleus will create a mixture of charged and neutral hadrons. The π^0 s will decay rapidly to photons and thus induce an electromagnetic shower. The charged hadrons pro-

¹⁶We are using natural units with $c = 1$ and we have assumed that the medium is non-dispersive.

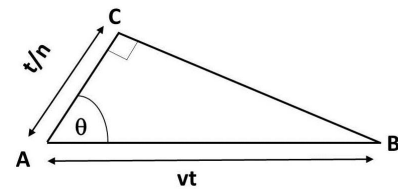


Fig. 4.7 Geometrical construction for the calculation of the Čerenkov angle.

¹⁷This provides another motivation for using high Z absorbers in an electromagnetic calorimeter (apart from wishing to limit the depth required for good shower containment); we use the fact that electromagnetic showers are contained in a shorter depth than hadronic showers and the separation is better for higher Z absorbers.

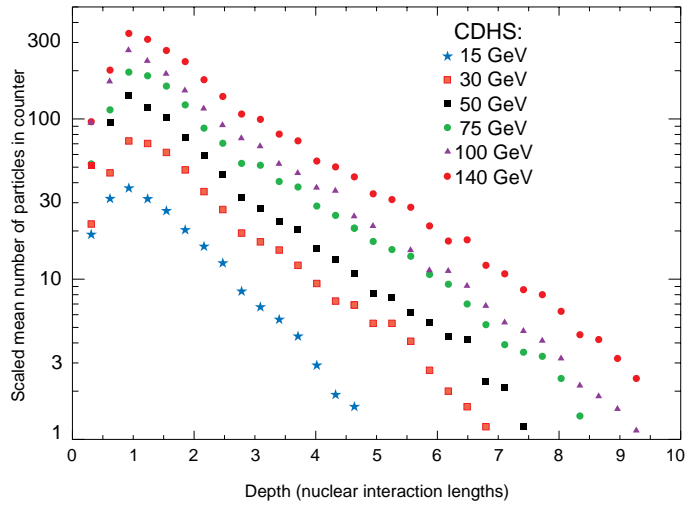


Fig. 4.8: Measured shower profiles for high energy pions in the CDHS detector.

Table 4.1: Radiation length (X_0) interaction length (λ_I) and density (ρ) for some elements.

Element	X_0 ($\text{g}^{-1} \text{cm}^2$)	λ_I ($\text{g}^{-1} \text{cm}^2$)	ρ (g cm^{-3})
Iron	13.84	132.1	7.874
Copper	12.86	137.3	8.960
Lead	6.37	199.6	11.350
Uranium	6.00	209.0	18.950

¹⁸For cost reasons, hadronic calorimeters are divided into alternating layers of 'passive' absorber and 'active' layers which detect the signal.

duced will penetrate further into the calorimeter and create secondary hadronic interactions, leading to the development of a shower deep into the calorimeter. The big difficulty with hadronic calorimetry is that a significant fraction of the energy goes into nuclear breakup and evaporating neutrons and protons from the nuclei. The resulting low energy neutrons and protons will be very heavily ionizing and lose energy rapidly. Typically this will occur in the passive absorber,¹⁸ producing no detectable signal in the 'active' layers. The low energy neutrons will scatter and thermalize on a timescale of μs , and so any photons produced from neutron-capture will be outside the time 'window' to collect the signal. The fraction of energy that is effectively 'lost' in a hadronic interaction due to these processes is very large (typically in the range 20% to 40%). The real problem is that there is a very large variation in this lost fraction from shower to shower, which greatly degrades the resolution of hadronic compared to electromagnetic calorimeters. The magnitude of the effect can be parameterized by the ratio of the response to electrons to that of hadrons, e/h . If e/h is significantly different from unity the calorimeter resolution will be limited and there will be sig-

nificant non-Gaussian fluctuations. Therefore several ideas have been pursued to try to achieve ‘compensating’ calorimeters in which $e/h \approx 1$ and these will be discussed in section 4.7.5.

4.4 Signal generation

In section 4.3 we have considered how particles lose energy in matter and create showers of secondary charged and neutral particles. We now need to examine how we can actually detect these secondary particles as well as the particles from the primary collision. In section 4.4.1 we will see how charged particles moving between electrodes induce currents, which we can amplify and readout with suitable electronics. Another approach considered in section 4.4.2 is to use scintillation light and in section 4.3.4 we will consider the use of Čerenkov and transition radiation. The scintillation and Čerenkov processes result in photons in the visible or UV wavelength, so in section 4.5 we review techniques to detect these photons.

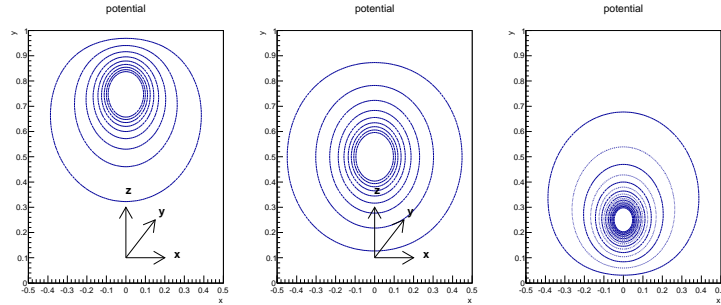
4.4.1 Moving charges

In this section we will study how to calculate the induced currents created by moving charges, which generate the electrical signals we can measure in detectors like wire chambers or silicon detectors. We will first calculate the induced current for a simple case and then discuss the general solution. Consider a charged particle held between two infinite parallel plate capacitors, with both plates grounded. The potential is given by the solution of Laplace’s equation [?], subject to the appropriate boundary conditions (the potential is 0 on the plates and looks like a point charge in the vicinity of the charge).

$$V(\rho, z) = (q/\epsilon_0\pi L) \sum_{n=1}^{n=\infty} \sin(n\pi z/L) \sin(n\pi z_0/L) K_0(n\pi\rho/L) \quad (4.13)$$

where z_0 is the distance from the lower plate to the point charge, L is the separation between the plates, and $\rho = \sqrt{(x^2 + y^2)}$ and x and y are the Cartesian coordinates of the point charge in the plane of the lower plate (see fig. 4.9) and K_0 is a modified Bessel function. The solutions for three locations of the charge are illustrated by the equipotentials shown in fig. 4.9.

The induced electric surface charge density on the conducting plate at $z = 0$ is given by $\sigma = \epsilon_0|E_z(z = 0)|$ where $\mathbf{E} = -\nabla V$ is the electric field evaluated at the edge of the conductor (z is the direction perpendicular to the conductor). When the charge is near the upper (lower) plate we can see that the equipotentials are more tightly packed near the upper (lower) plate. Therefore when the charge is near the upper (lower) plate the E field will be larger nearer the upper (lower) plate and hence there will be a larger induced charge on the upper (lower) plate. The fields and induced charges are obviously symmetric when the charge is equidistant



(a) charge near upper plate (b) charge near centre (c) charge near lower plate

Fig. 4.9: Equipotentials (arbitrary units) for a point charge at three different locations in a parallel plate capacitor. The equipotentials near the point charge are omitted for clarity.

from the two plates. Now let us imagine moving the charge from near the upper plate to near the lower plate. Initially most of the induced charge will be on the upper plate but this will gradually change and at the end most of the induced charge will be on the lower plate. This then looks like a current flowing between the two conductor plates. This is a qualitative example of the fundamental result in detector physics; moving charges between conducting electrodes induce currents¹⁹. This current can be amplified and digitized by appropriate readout electronics.

¹⁹Note that the induced signal occurs as long as the charge is moving and stops when the charges are collected on the electrodes. A popular misconception is that the signal only arises when the charge is ‘collected’ at an electrode.

Now that we have seen a qualitative description of the physics of induced charges, we can look at the quantitative solution. Taking the derivative in the z direction of the potential (eqn 4.13) we can determine the induced surface charge density on the upper and lower plates using Gauss’s law.

$$\begin{aligned}\sigma(\rho, z = 0) &= -(4q/L) \sum_{n=1}^{\infty} \frac{n\pi}{L} \sin(n\pi z_0/L) K_0(n\pi\rho/L) \quad (4.14) \\ \sigma(\rho, z = L) &= (4q/L) \sum_{n=1}^{\infty} \frac{n\pi}{L} (-1)^n \sin(n\pi z_0/L) K_0(n\pi\rho/L).\end{aligned}$$

We can integrate the surface charge density to find the total charge induced on the upper plate as

$$\begin{aligned}Q_U &= 2\pi \int_0^{\infty} \sigma(\rho, z = L) \rho d\rho \quad (4.15) \\ &= (2q/L) \sum_{n=1}^{\infty} \frac{L}{n\pi} (-1)^n \sin(n\pi z_0/L) \int_0^{\infty} x K_0(x) dx.\end{aligned}$$

The integral is equal to unity so

$$Q_U = (2q/\pi) \sum_{n=1}^{\infty} \frac{L}{n\pi} (-1)^n \sin(n\pi z_0/L). \quad (4.16)$$

We can see that the infinite sum is related to a Fourier series (see exercise 4.3) so that

$$Q_U = -qz_0/L. \quad (4.17)$$

We can calculate the surface charge on the lower plate at $z = 0$ by the same method to obtain²⁰

$$Q_L = -q(L - z_0)/L. \quad (4.18)$$

Now let the charge between the capacitor plates be moving with a speed v in the negative y -direction. The induced charge flows from the upper to the lower plate and the current (while the charge is moving) is given by the rate of change of charge as

$$I = -qv/L. \quad (4.19)$$

We have determined the induced current for the simplest possible geometry. A more general solution to the calculation of the induced current which is indispensable for understanding realistic detector geometries is provided by Ramo's theorem²¹. This will provide us with a simple method for calculating the induced currents from any movements of charges and is therefore of fundamental importance in detector physics. First set the potential on the electrode being considered to 1V and apply 0V to all other electrodes and calculate the potential Φ by solving Laplace's equation subject to these boundary conditions. The 'weighting' field²² is defined as $\mathbf{E}_W = -\nabla\Phi$. The current induced on this electrode, caused by the motion of n charges, each with a charge q moving with velocity \mathbf{v}_i is given by

$$i = -\sum_i q_i \mathbf{v}_i \cdot \mathbf{E}_W. \quad (4.20)$$

The velocity depends on the real electric field not the weighting field²³. As a simple 'sanity check' we can now use Ramo's theorem to calculate the induced current for the case of a point charge between the plates of an infinite parallel plate capacitor and compare the result we obtained previously. For this geometry, if we apply 1V on one electrode and 0V on the other electrode, the weighting field is uniform and has a magnitude of $1/L$. For a point charge, q , moving with velocity v parallel to this weighting field, we simply obtain the induced current from eqn 4.20 as

$$I = -qv/L. \quad (4.21)$$

which is in agreement with eqn 4.19²⁴.

4.4.2 Scintillators

Scintillators are materials in which ionizing particles can cause scintillation light, which can be detected by photo-detectors. There are two broad classes of scintillator, organic or inorganic. A common example of an organic scintillator is polystyrene. In an organic scintillator, molecule

²⁰The total induced charge on the two plates is $-q$ as expected.

²¹See Speiler in further reading for a derivation of Ramo's theorem.

²²Please note that this field is not the same as the electric field and does not even have the same dimensions.

²³only in the case of two electrode systems does the weighting field have the same form as the physical electric field.

²⁴This result is independent of what forces cause the charge to move with a velocity v . In a particle detector, the motion is due to the applied electric and magnetic fields and the interactions of the moving charge with atoms or molecules in the detector.

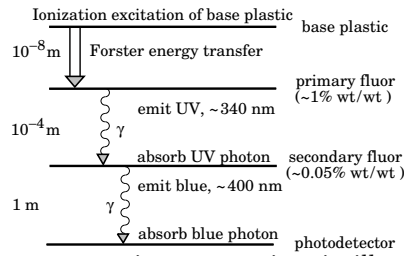


Fig. 4.10: Scintillation and fluorescence steps in an organic scintillator. Typical values are given for the wavelength and absorption length of the photons, The first step in the process called ‘Foerster energy transfer’ does not involve photon emission but is a dipole-dipole interaction between the base and the primary fluor.

²⁵This is clearly a problem for an application requiring large area scintillators.

are lifted into an excited state by an ionizing particle and they can then emit scintillation photons (typically in the UV). The problem with this is that the reverse reaction has a large cross section, so these UV photons will be rapidly absorbed²⁵. Therefore a dopant is introduced so that the photons are absorbed by a fluorescent molecule (‘fluor’). The fluor can then rapidly decay to a lower energy in a radiative decays, emitting longer wavelength photons. This increases the attenuation length but it still usually too short for practical applications. Therefore a secondary fluor is used to shift the photons into the visible wavelength range and these photons can have a suitably long attenuation length. The typical scintillation and fluorescence process ([?]) are illustrated in fig. 4.10. This type of organic scintillator is often used in sampling calorimeters (see sec 4.7).

A classic example of an inorganic scintillator is NaI(Tl). A high energy particle can excite an electron from the valence to the conduction band. The electron can drop from the conduction to the valence level with the emission of a photon. However the reverse process will result in too short an attenuation length for a useful detector. Therefore a different process is used in which high energy particles create excitons (loosely bound states of an electron and a hole). An exciton can move through the crystal until it is captured by an impurity state (created by doping with Tl) which can then decay via emission of a photon thus creating scintillation light²⁶. This has the advantage of high density²⁷. and has a very good yield for scintillation light. This scintillator is still used in many applications and it was used in older particle physics detectors. The problem is that it is too slow for use at modern colliders because the scintillation decay time is ≈ 250 nss.²⁸. To use an inorganic scintillator at LHC, we need a very fast decay time and the scintillator must be very tolerant to radiation²⁹. CMS have developed such a scintillator, PbWO₄ and its use in the CMS electromagnetic calorimeter will be described in sec. 4.7.

²⁶As the doping concentration is relatively low, the probability of the scintillation light being reabsorbed in the crystal is very low, i.e. the crystal is transparent at this wavelength.

²⁷A higher density allows for the construction of a more compact calorimeter, which reduces the cost.

²⁸This is much longer than the time between collisions at the LHC of 25 ns.

²⁹Most scintillators would become opaque after exposure to LHC radiation levels.

4.5 Photon Detection

We have seen that scintillation and Čerenkov radiation result in photons in the range from the optical to the UV and we ultimately have to convert the photons into an electrical signal which can be digitized and readout. The traditional method is based on photomultipliers (PMTs) but another technique which is becoming increasingly common uses avalanche photodiodes. A schematic view of a photomultiplier coupled to scintillator is illustrated in fig 4.11. A photomultiplier has a photocathode.³⁰. When a photon with an energy greater than the work

³⁰Usually containing two alkali elements to obtain the best quantum efficiency.

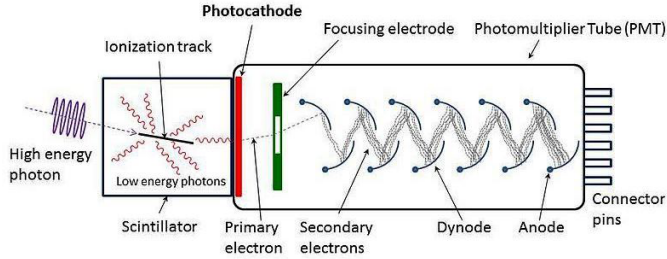


Fig. 4.11: Schematic view of a photomultiplier and the main processes. The primary photon is emitted from the photocathode and is accelerated and focused until it hits the first dynode. It then liberates many secondary electrons which are accelerated to the next dynode. The resulting induced current is detected on the anode.

function hits the photocathode it can emit an electron by the photoelectric effect. The resulting electron is then accelerated by an applied electric field until it hits the first dynode³¹. This will cause the emission of several secondary electrons (the electron has been accelerated so it has sufficient energy to do this). The secondary electrons are similarly accelerated and strike the second dynode. This clearly multiplies the number of electrons (hence the name photomultiplier). Several stage of dynodes are used and it is easy to obtain a very large gain (of the order of 10^6 or more). A single photon thus creates a large pulse of electrons which is easy to detect and digitize. One disadvantage of PMTs is that they do not work in large magnetic fields³².

The simplest solid state photo-detector is a photodiode. In a photodiode, photons create electron-hole pairs in a detector working with the same principles as that of a silicon detector³³ (see section 4.6.2). The problem is that the small signal results in a low signal-to-noise ratio. In an Avalanche Photo Diode (APD) the electric field is large enough that electron acquire sufficient energy to create further electron-hole pairs, this leading to an ‘avalanche’ effect. This avalanche process therefore creates an intrinsic gain in the device which results in APDs having better resolution for small calorimeter signals than simple photodiodes. This requires larger reverse bias to be applied, typically ~ 100 V which results an avalanche gain in the range 10-100. The gain of an APD is more sensitive to the applied bias voltage and the temperature than simple photodiodes. In addition the design needs to ensure that the avalanche does not lead to electrical breakdown. One key advantage of APDs for particle physics applications is that they are insensitive to applied magnetic fields.

4.6 Detectors for charged particle tracks

The traditional technology for tracking uses wire chambers. These have been largely replaced by silicon detectors in the inner detectors for the LHC general purpose detectors. However the cost of silicon detectors would be prohibitive for the very large area detectors needed for the

³¹Additional electrodes act as electrostatic focusing elements to increase the fraction of electrons collected at the first dynode.

³²For operation in moderate magnetic fields, the PMT can be shielded from the magnetic field by ‘mu metal’ shields. Mu-metal is an alloy with an exceptionally large relative permeability. However saturation effects, prevent this technique from working in high magnetic fields.

³³Silicon is one possible semiconductor that can be used for photodiodes but there are photodiodes made from other semiconductors such as GaAs or InGaAs. The optimal choice for any application depends on several factors including, wavelength, speed of response and cost.

muon spectrometers, therefore wire chambers are the only practical technology for these systems.

4.6.1 Wire chambers

A primary high energy charged particle passing through a gas will create a few electron-ion pairs by ionization. In order to create a sufficiently large signal (i.e. greater than the electronic noise of an amplifier) we need to use an avalanche process. We will therefore start by considering the ‘gas gain’ caused by an avalanche. We will then consider the simple proportional wire chamber and then look at a ‘drift’ chamber.

Gas Gain

At sufficiently high electric fields (~ 100 kV/cm) electrons drifting in an electric field acquire sufficient energy to cause further ionization in the gas and thus allow for the possibility of an avalanche process which can result in a very large increase in the number of electron-ion pairs. We define the gas gain $G = N/N_0$ where $N(N_0)$ is the final (initial) number of electron-ion pairs. The change in N with distance traveled ds is given by

$$dN = N\alpha ds \quad (4.22)$$

where α is called the first Townsend coefficient and has to be measured experimentally. We can integrate equation 4.22 for the gas gain

$$\begin{aligned} G = N/N_0 &= \exp \left\{ \int \alpha ds \right\} \\ &= \exp \left\{ \int_{E_{min}}^{E_{max}} \frac{\alpha}{dE/ds} dE \right\} \end{aligned} \quad (4.23)$$

where E is the electric field, E_{min} is the value of E at the start of the avalanche and E_{max} is the value at the end of the avalanche (e.g. at the wire in a wire chamber). The value of E_{min} is simply related to the mean free path for electrons λ and the average ionization energy I by conservation of energy $eE_{min}\lambda = I$.

We will now consider the general features of the gas gain as a function of the applied voltage across a chamber as illustrated in fig. 4.12. At very low voltages the electrons recombine with ions before they are collected. At higher voltages we can distinguish different regions:

- **Ionization chamber.** In this region the electrons do not acquire sufficient energy to start an avalanche and we just see the signal from the primary electron-ion pairs, i.e. there is no gas gain;
- **Proportional regime.** In the ‘proportional’ regime there is gas gain and the number of electron-ion pairs created by the avalanche is proportional to the number of primary electron-ion pairs. Typical values of gas gain are in the range 10^4 to 10^5 ;

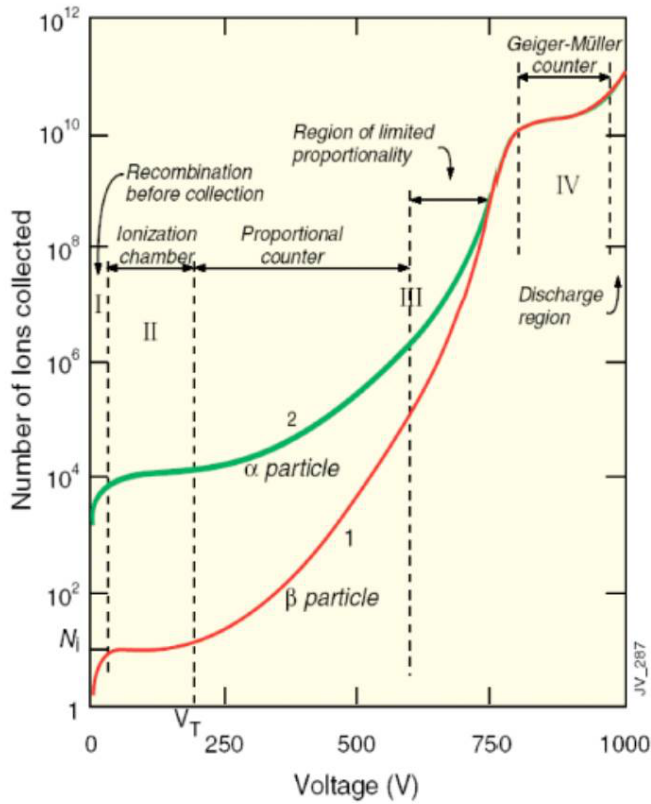


Fig. 4.12: Variation in gas gain as a function of applied voltage.

- **Limited proportionality.** At higher voltages, the density of electron-ion pairs is so high that after the lighter electrons have drifted some distance the net space charge density is so large that it decreases the field, thus lowering the gain;
- **Geiger-Muller mode** at the highest voltages we have the Geiger-Muller mode with very large gains $\sim 10^{10}$. In order to operate in this regime we require a very large series resistance for the high voltage to lower the voltage when the current gets too high to avoid complete electrical breakdown. This creates a long recovery time between pulses and is therefore not useful for high rate applications.

The actual calculation of the gas gain depends on dE/ds which clearly depends on the geometry used to create the field. We can calculate the gas gain for the case of the proportional wire chamber (see sec. 4.6.1). Substituting for the electric field from eqn. 4.26 into the gas gain equa-

tion (eqn. 4.24) we can show that the gas gain is

$$G = \exp \left\{ V \int_{E_{min}}^{E_a} \frac{\alpha(E)}{3 \ln(b/a) E^2} dE \right\}. \quad (4.24)$$

If we use the linear approximation that $\alpha(E) \approx \beta E$ where β is an empirical constant then we can integrate eqn. 4.24 to show that

$$G = \exp \left\{ \frac{\beta V}{3a \ln(b/a)} \ln \left(\frac{V}{a E_{min} \ln(b/a)} \right) \right\}. \quad (4.25)$$

This allows us to understand the rapid and approximately exponential rise of the gas gain with applied voltage that we saw in fig. 4.12 for the proportional regime.

Proportional wire chambers

The geometry of a cylindrical proportional chamber is sketched in fig. 4.13. In a typical arrangement, there is a thin anode wire at a high voltage (HV) potential of a few kV on the axis and the cylindrical cathode is at ground potential. The wire has a radius of 10 to 20 μm . Assuming that the length of the wire is much longer than the diameter (a very good approximation), we can easily calculate the magnitude of the electric field from Gauss's law. Taking a cylindrical surface around the wire we can show that the magnitude of the electric field is given by

$$|\mathbf{E}| = \frac{V}{\ln(b/a)r} \quad (4.26)$$

where V is the potential difference between the anode and cathode, a (b) is the radius of the anode (cathode) and r is the radial distance from the centre of the anode wire, see fig. 4.14. The cell is filled with a gas. A common, cheap and safe, choice of the gas is 9 to 1 argon and CO_2 mixture³⁴. A charged particle crossing the cell ionizes the gas creating about 40 to 60 electron pairs per cm. This number of electron-ion pairs is then increased by a factor of 2 to 3 because some electrons have enough energy to ionize the gas further. Electrons drift towards the anode and much slower (massive) ions drift towards the cathode in a diffusion like process³⁵. Very close to the anode, a few times the anode wire diameter, the electric field is high enough (thin anode wire) to accelerate the drifting electrons to energies allowing for further gas ionization and this leads to an avalanche process (see section 4.6.1) There is also recombination of electrons and ions with emission of UV photons. Those photons, if not absorbed, could eject electrons from the cathode leading to continues electric discharge. The role of the CO_2 (or another gas with molecules with many degrees of freedom) is to absorb those UV photons and transform their energies to molecular vibrations or rotations, which then decay via emission of longer wavelength photons. These longer wavelengths photons have too low energy to eject electrons from the cathode. In this typical arrangement, the cell operates in the proportional regime.

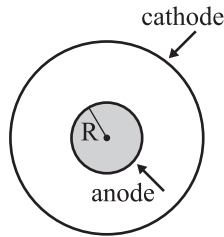


Fig. 4.13 A fundamental cell of a wire chamber. Not too scale.

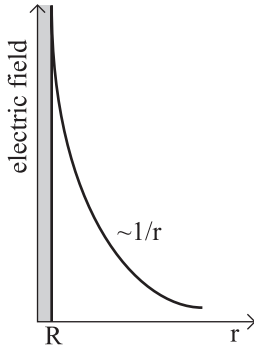


Fig. 4.14 Electric field inside the fundamental cell of a wire chamber.

³⁴A noble gas has the advantage that it is chemically inert, so the electrons liberated by ionization will be able to travel without being absorbed. The role of the CO_2 is explained below.

³⁵Electrons and positive ions are accelerated by the electric field but undergo many collisions with the gas atoms. This results in the electrons and positive ions having a uniform 'drift velocity' superimposed on the random motion as in a conductor. For our purposes we can ignore the random motion and just consider the drift velocity. However the random motion contributes to diffusion and is one of the factors limiting the resolution of wire chambers

We will consider two common types of wire chambers³⁶ : multi-wire proportional chambers (MWPC) and proportional drift chambers (drift chamber). A typical example of an MWPC, as sketched in fig. 4.15, consists of a plane of anode wires between two planes of cathodes (sometimes cathode wires). Such chambers are often used in fixed target experiments where charged particles are crossing chambers close to perpendicular to their anode planes. If the spacing between anode wires is d , and a simple binary readout is used (i.e. a wire either records a hit or no-hit) the resolution of reconstructed points on the charged particle trajectory is $d/\sqrt{12}$ (see exercise 4.12). The separation between anode wires cannot be too small because of the large electrostatic forces on the wires. The wires are held under tension to prevent neighbouring wires touching but this imposes a minimum separation of a few mm. Drift chambers have better space resolution, down to about $50 \mu\text{m}$. A drift chamber in the barrel of a collider (head on collisions) detector has a cylindrical structure. Anode wires are parallel to the chamber axis (parallel to the beam direction) and each anode wire is surrounded by cathode wires creating a fundamental cell as sketched in fig. 4.16. Such a cell might be several cm across, so the anode (or sense) wires are far apart from each other in comparison with an MWPC arrangement. This arrangement provides position measurements in the plane perpendicular to the beam axis. The trick is to measure the electrons' drift time. Using a signal from a fast independent detector like a scintillator, measuring precisely when particles in colliding beams interacted producing charged particles crossing the drift chamber, one can measure the time between the primary ionization and the leading edge of a signal from an anode wire. The measurement of position along the beam direction can be done by different techniques. One method is to use anode wires at a small angle to the beam direction, which allows for 'stereo' reconstruction of the distance along the beam axis. The geometry of the fundamental cell as well as the gas composition need to be chosen carefully, so the drift velocity³⁷ of electrons is as uniform as possible across the cell, allowing for precise measurement of the location where the primary ionization took place; calculating it from the drift time and the drift velocity³⁸. In older experiments the time of the signal was measured relative to an independent signal from a fast detector like a scintillator. At the LHC we do not need an external timing detector because we can use the LHC machine clock running at 40.008 MHz.

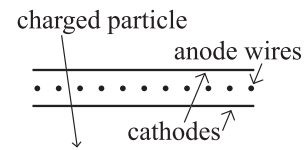


Fig. 4.15 A MWPC.

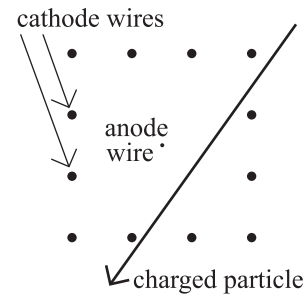


Fig. 4.16 A drift chamber and its fundamental cells.

³⁷Typically a few cm per μs .

³⁸It is often a little more complicated because in the presence of a magnetic field, electrons don't drift along lines of the electric field in the drift chamber but at an angle, known as the Lorentz angle to them.

Signals and readout for wire chambers

In this section we will calculate the induced current in a cylindrical wire chamber. The electrons drifting towards the anode will create an avalanche very close to the anode wire. To a first approximation we can neglect the induced signal from the flow of electrons because they travel such a short distance. We can then calculate the induced current as the positive ions drift away from the wire to the anode.

We can easily calculate the current induced by the motion of a single

ion in the simple cylindrical wire chamber using eqn 4.20. As this is a two electrode geometry, we can read off the weighting field from the actual electric field by setting the voltage across the chamber to be 1V and therefore from eqn 4.26

$$|\mathbf{E}_w| = \frac{1}{\ln(b/a)r}. \tag{4.27}$$

The drift velocity of the ion v_d is related to the electric field, \mathbf{E} by $\mathbf{v}_d = \mu\mathbf{E}$ where μ is the ion mobility. We will assume that the mobility is constant. If the number of electron-ion pairs created by the avalanche from a single primary electron is N_{Tot} the induced current (eqn 4.20) is³⁹ then

$$I = -N_{Tot}e \frac{v_d}{\ln(b/a)r}. \tag{4.28}$$

Substituting for the electric field for this geometry we get the ion speed as

$$v_d = \frac{dr}{dt} = \frac{\mu V_0}{r \ln(b/a)} \tag{4.29}$$

multiplying both sides by r we can integrate eqn 4.29 and solve for r

$$r = a[1 + (t/t_0)]^{1/2} \tag{4.30}$$

where $t_0 = a^2 \ln(b/a)/(2\mu V_0)$. Substituting from eqn 4.29 into eqn 4.28 we get

$$I(t) = -N_{Tot}e \frac{1}{\ln(b/a)r} \frac{\mu V_0}{\ln(b/a)r}. \tag{4.31}$$

Substituting for r from eqn 4.30 into eqn 4.31 we can calculate the induced current as a function of time

$$I(t) = \frac{-N_{Tot}e}{2 \ln(b/a)} \frac{1}{t + t_0}. \tag{4.32}$$

This current flows up to the time (t_{max}) that the positive ions reach the anode. We can calculate t_{max} from eqn 4.30 by setting $r(t_{max}) = b$

$$t_{max} = (b^2 - a^2) \frac{\ln(b/a)}{2\mu V_0}. \tag{4.33}$$

We can calculate t_0 and t_{max} for typical conditions (see exercise 4.11) to find $t_0 \sim 1 \text{ ns}$ and $t_{max} \sim 100 \mu s$. This pulse shape is illustrated in fig. 4.17

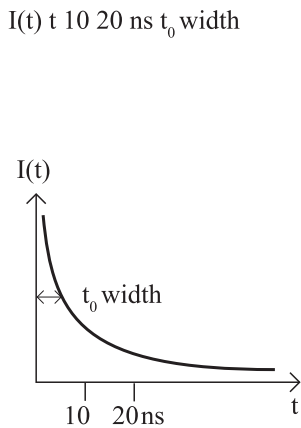


Fig. 4.17 Typical pulse shape from a cylindrical wire chamber.

Eqn 4.32 shows that the current pulse has a fast peak and then a very slow ‘tail’. For a high rate application such as a collider detector we need fast pulses. We can produce a fast pulse by suitable ‘pulse shaping’, this is done by filtering in frequency space, so as to remove the low frequency signals. A typical electronic readout circuit is sketched in fig 4.18 R_1 is very large ($M\Omega$), thus protecting the anode wires from large currents (which otherwise could flow, from the high voltage power supply to the ground, due to occasional electric discharges; sparks) which might melt them (they are thin). R_2C_2 and R_2C_1 are time constants, small enough to allow a fast current flow through R_2 , the input resistance of a pre-amplifier connected to the anode wire; isolated from the HV by the C_2 capacitor.

³⁹The signal from a single electron is too small to measure. However with the large gas amplification, the signal can be measured by a suitable low noise amplifier.

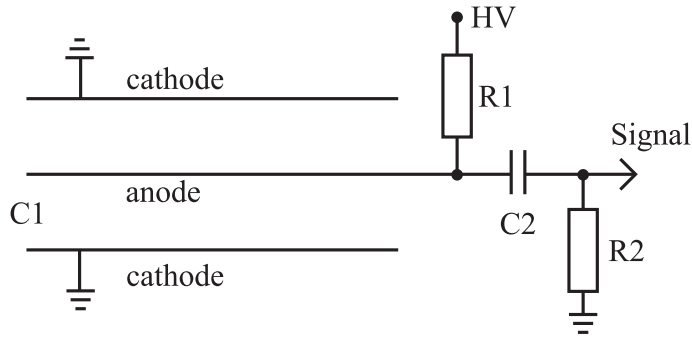


Fig. 4.18: Fundamental cell readout circuit.

4.6.2 Silicon Detectors

Silicon strip detectors as well as silicon pixel detectors are playing an increasingly important role in tracking. The functioning of silicon detectors is based on the fact that silicon is a semiconductor with a bandgap of 1.1 eV. A high energy charged particle traversing silicon will interact with the silicon to create electron-hole pairs. However most of the energy goes into phonons, so the average energy lost per electron-hole pair created is significantly larger, about 3.6 eV. This results in about 80 electron-hole pairs per μm for a minimum ionizing particle. If no external field is applied the electron-hole pairs would move apart slowly due to diffusion, however this process is too slow for most applications in particle detectors. Therefore an electric field is applied to separate the electrons and the holes. This motion of the electrons and holes causes an induced current to flow in the external circuit as discussed in section 4.4

Even in high purity, high resistivity silicon, the presence of a strong electric field would result in an unacceptably large leakage current, i.e. current flowing even without the presence of the charged particle⁴⁰. This problem is solved by making a *pn* junction, which forms a diode junction. When a reverse bias is applied to the diode, the free electrons are removed from the *n* doped region, creating a ‘depletion’ region, in which there is a very low density of free carriers, thus allowing a large electric field to be applied, without paying the price of the unwanted large leakage current⁴¹. How thick does the silicon have to be to create a big enough signal? There is actually no correct answer to this question because it depends on the amplifier, but a typical choice is $300\ \mu\text{m}$ which results in a signal of about 25,000 electron-hole pairs for a minimum ionizing particle. The next question to consider is how large an electric field do we need to fully deplete the silicon? We can answer this question starting from Poisson’s equation for the potential V , in terms of the charge density ρ and the dielectric constant ϵ

$$\nabla^2 V = \rho/\epsilon. \quad (4.34)$$

If we assuming an effectively one-dimensional diode, and N is the net volume number density of charges, we can use eqn 4.34 to calculate the

⁴⁰The leakage current represents a noise source which if it is too large will swamp the signal. In addition the leakage current will lead to local heating of the silicon and it is difficult to remove this heat without adding excess material.

⁴¹Thermal generation of electron-hole pairs will always occur but the resulting leakage current is usually acceptable or if not it can be reduced by cooling the silicon.

potential as a function of the distance x

$$\frac{d^2V}{dx^2} + \frac{Ne}{\epsilon} = 0. \quad (4.35)$$

where e is the electron charge and ϵ is the permittivity of silicon. We will consider a detector with p strips in n bulk silicon. In this case the p region is much more heavily doped than the n region, so we only need to consider the n doped region. On applying the reverse bias, we remove all the free electrons from the n -doped region, which leaves behind a fixed space charge density. Therefore integrating eqn 4.35 gives⁴²

⁴²This is just equal to minus the electric field.

$$\frac{dV}{dx} = -\frac{N_d e}{\epsilon}(x - x_n). \quad (4.36)$$

where N_d is the donor (electron) density and x_n is the limit of the depletion region. Integrating eqn 4.36 gives

$$V = \left(-\frac{N_d e}{\epsilon}\right)\left(\frac{x^2}{2} - xx_n\right). \quad (4.37)$$

Therefore the total voltage applied across the depletion region is found by setting $x = x_n$ is

$$V_{bias} = \frac{N_d e}{\epsilon} \frac{x_n^2}{2}. \quad (4.38)$$

Equation 4.38 shows why we need high purity silicon to make good detectors because impurities contribute to N_d and hence cause an increase in the bias voltage required for full depletion⁴³. With typical detector grade silicon, a 300 μm thick silicon detector requires a bias voltage of about 50V which results in an electric field of about $1.7 \cdot 10^5 \text{V/m}$. We can calculate the drift velocities for electrons and holes

⁴³Too high a bias voltage will result in electrical breakdown in the cables or the silicon detector itself.

$$v_{drift} = \mu E \quad (4.39)$$

where μ is the mobility and E is the electric field. From the measured mobilities, this gives maximum drift times of 13 (40) ns for electrons (holes), which are comparable to the time between bunch crossings at the LHC of 25 ns.⁴⁴ Great care is needed in the design of silicon detectors because too large electric fields can lead to electrons gaining enough energy to cause secondary ionization which leads to an avalanche effect and hence results in electrical breakdown⁴⁵.

⁴⁴Detectors are typically operated at higher bias voltages to speed up the signal collection.

⁴⁵Electrical breakdown will start in the region of highest electric field. Any very small scale non-uniformities in the electrode structure can cause enhanced electric fields and hence lead to electrical breakdown, even at relatively low bias voltages.

⁴⁶In normal operation there is no equivalent of gas gain in silicon detectors although devices like avalanche photodiodes can be operated at sufficient voltage for amplification to occur.

⁴⁷At nominal LHC operating conditions, the bunch crossings occur every 25 ns.

⁴⁸The electrical power consumption must be minimized because if more heat is generated, the cooling system will need to be more massive, which degrades the resolution of the tracker and creates unwanted secondary interactions in the tracker.

In order to understand if this small signal⁴⁶ can be detected it is essential to consider all sources of electronic noise. This is discussed in detail in Speiler in further reading from which we see that we need to have low capacitance detectors. For high rate applications, such as for silicon trackers at the LHC, we need to minimize ‘pile-up’ backgrounds from hits in previous bunch crossings⁴⁷ generating spurious hits in the triggered bunch crossing. This implies that the ‘shaping time’ of the electronics should be not more than O(25 ns). The challenge is to design low-noise amplifiers which are sufficiently fast and consume low power⁴⁸.

Radiation Damage

One of the difficulties with the application of silicon detectors in particle physics, particularly at the LHC is the effects of radiation damage. At a radius of 30 cm from the beam line, the expected ionising dose over the detector lifetime is 100 kGy(Si)⁴⁹. High energy particles can displace silicon atoms from their lattice sites, creating complex defects which result in mid-band gap states (i.e. between the valence and conduction band). This makes it much easier for thermal generation to promote an electron from the valence to the conduction band. This greatly increases the leakage current. The leakage current is strongly dependent on the temperature T

$$I_{leak}(T) = AT^2 \exp(-E_g/2k_B T) \quad (4.40)$$

where k_B is the Boltzmann constant and E_g is the band gap, which for silicon is $E_g = 1.1eV$ ⁵⁰. Therefore the leakage current can be very efficiently suppressed by cooling the silicon. These mid band gap states act like extra acceptors and thus change the effective dopant concentration⁵¹. From eqn 4.38 we can see that an increase in the effective dopant concentration will result in detectors requiring higher bias voltages to be fully depleted. The electrical breakdown of detectors at very high voltages, therefore sets the scale for the maximum radiation doses that can be tolerated. In addition some of the extra states can cause 'charge trapping', which looks like a signal loss.

Silicon Systems

The spatial resolution of a silicon detector is largely determined by the segmentation of the silicon into individual detector channels. If the width of a detector segment is x , and if a particle only causes a hit in a single channel the spatial resolution in this direction is $x/\sqrt{12}$ ⁵². There are generally two classes of silicon detector systems, strips and pixels.

Strip Systems

A very simplified schematic cross section of part of a generic silicon strip detector is shown in fig. 4.19. A positive high voltage is applied to the 'backside' via the Al contact which depletes the n -bulk silicon. Electron-hole pairs created by ionizing particles drift in the electric field and the current induces signals on the readout electrodes. The signal electrodes are AC coupled to the Al strips (using the SiO₂ as an insulator), which are then connected to the preamplifiers in the readout ASIC (application specific integrated circuit). The noise increases with the detector capacitance (see Speiler in further reading for an explanation), therefore for high rate applications such as the LHC, we must minimize any stray capacitance between the detector and the amplifier. The connection is done with 'wire bonds', typically a few mm long and 25 μm thick aluminum wire. These thin bond wires can be ultrasonically bonded to pads on the detector and on the readout ASIC. This allows for a very

⁴⁹Gy(Si) is the SI unit of dose and corresponds to 1 Joule of energy deposited per kg of Si. To set the scale a dose of 100 kGy(Si) corresponds to about 10⁹ lung X-rays.

⁵⁰A useful rule of thumb is that the leakage current doubles for every 7K increase in temperature.

⁵¹With sufficient damage this can cause n -type silicon to change to p -type silicon, a process called type inversion. However detectors can operate satisfactorily after type inversion.

⁵²Improved resolution can be achieved by using signals in neighbouring channels. The amount of charge sharing with neighbouring channels gives extra information as to the location of the 'hit'.

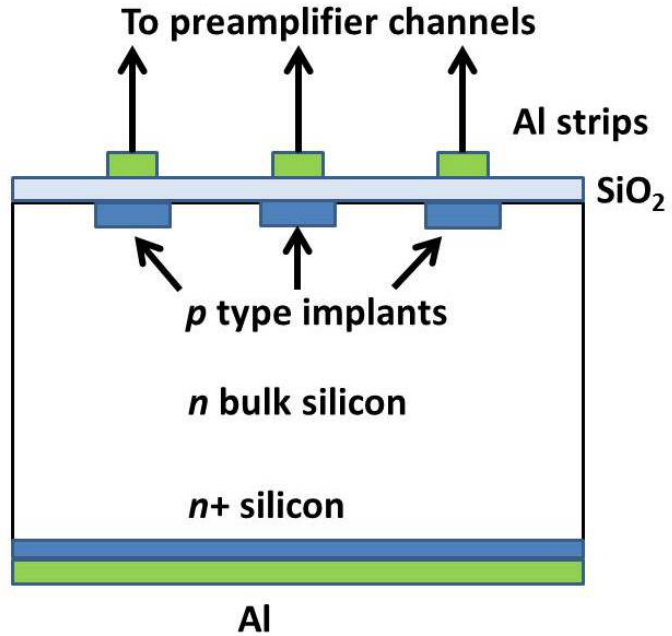


Fig. 4.19: Schematic cross section through a silicon micro-strip detector with p implants in an n -bulk silicon.

⁵³We also need to create a DC return path for the current and this requires a large value resistor, so that the fast signal flows across the capacitor. This can be achieved with polysilicon resistors inside the silicon detector itself.

⁵⁴The largest wafers that are used are 6 inches in diameter.

⁵⁵This has the disadvantage that it creates ambiguities if more than one particle hit a sensor.

⁵⁶In the ATLAS case a discriminator is used to determine if hits are above threshold, so the output data is digital. In the CMS tracker, the signal amplitude is transmitted off-detector via analogue optical links.

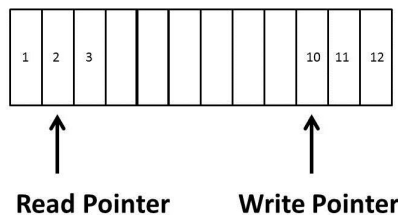


Fig. 4.20 Principle of a pipelined memory. At each clock cycle, data is written into the cell defined by the write pointer. This pointer is advanced by one cell every clock cycle and after it gets to the last cell, it cycles back to the first. The read pointer follows a fixed number of clock cycles behind the write pointer. The time delay between

short connection between the detector and the amplifier, which introduces much less capacitance than a longer wire cable.⁵³

In a strip detector, the silicon wafer is divided into long narrow strips, with typical strip widths in the range of 50 to 100 μm ⁵⁴. This is used to obtain good precision in the bending plane of the magnetic field. Modest resolution (order 1 mm) in the orthogonal direction is achieved by having half the sensors with a small stereo angle⁵⁵.

The amplifiers are in custom designed ASICs. As the time taken for the first level trigger (L1) (see section 4.10) is $O(\mu\text{s})$ which is much longer than the time between bunch crossings (25 ns at the nominal LHC operating condition) the data must be kept on-detector until the trigger decision is made. This is achieved with ‘pipeline’ memory in which the data from each strip for each bunch crossing is stored in different memory elements (see fig. 4.20). If the L1 rejects the event, the corresponding data can be overwritten. If the event is triggered at L1, the corresponding data is readout via optical links⁵⁶.

A schematic view of an ATLAS SemiConductor Tracker (SCT) module is shown in fig. 4.21. The module consists of two pairs of silicon wafers glued together to make a double sided module. The ASICs are mounted on flexible copper-kapton circuits. The beryllia ‘ear’ at the side allows the module to make good thermal contact to the cooling tube. The coolant used is C_3F_8 as this provides very efficient two phase cooling, i.e. the heat from the ASICs and the silicon detectors is used to evaporate liquid C_3F_8 . These are very large systems with 60 m^2 of silicon detectors for ATLAS and 200 m^2 in the case of CMS. The modules have to be held

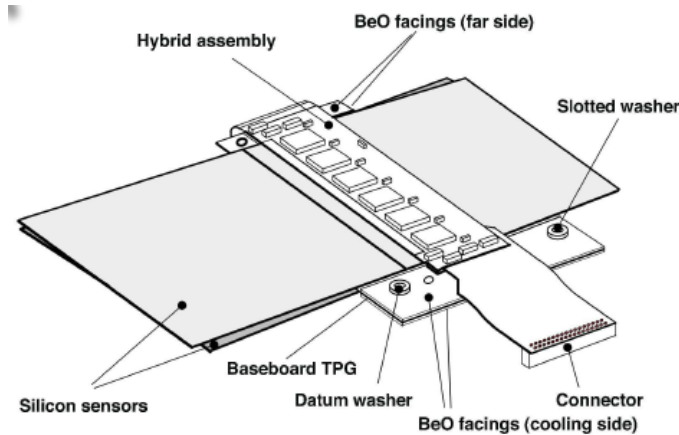


Fig. 4.21: Schematic view of an SCT module.

rigidly in place to benefit from the high intrinsic spatial resolution but the material must be minimized because any material causes multiple scattering of all charged particles and results in electrons and photons starting electromagnetic showers before the calorimeter. Therefore each module is mounted on carbon-fibre support structures as this provided the best ratio of stiffness to weight.

Pixel Systems

In silicon pixel detectors, the silicon is divided into much smaller areas, for example the ATLAS pixel detector the dimensions of individual pixels are $50\ \mu\text{m}$ by $400\ \mu\text{m}$. The smaller dimension is in the bending plane of the magnetic field to optimize the momentum resolution. The first advantage of pixel over strip detectors is that they provide unambiguous high precision space points. In addition the ‘occupancies’ (i.e. fraction of detector elements which are hit in a given event) are much lower for pixel detectors than strips. This is vital for pattern recognition at the LHC which has to reconstruct tracks in the presence of ‘pile-up’ background from about 25 collisions in the same bunch crossing. The small area of the pixels means that the detector capacitance is very low, which allows very low noise to be achieved (see Spieler in further reading). However this requires minimization of stray capacitance between the silicon pixel and the amplifier in the ASIC. One of the main difficulties of pixel systems is to make the electrical connection from each silicon pixel to a unique channel of the readout ASIC, without introducing any significant capacitance. This is achieved by ‘bump bonding’⁵⁷. The much larger number of channels in pixel systems than strips, requires more sophisticated data processing in the ASICs⁵⁸. Other system aspects are similar for pixels as for strips.

Pixel systems offer many performance advantages over strips, but as the electronics covers essentially the full sensitive area, a layer of pixel detector will have more material than an equivalent layer of strips. In addition pixel detectors are significantly more expensive than a strip

⁵⁷In this process indium solder is deposited on metalised pads on the pixel, heated in a reflow process to form hemispherical solder balls, the detector is then flipped and positioned very precisely over a flexible circuit with the readout ASICs already mounted. A further reflow of the solder results in an electrical connection between the pixels and the amplifiers in the readout ASICs. It is difficult to achieve a high yield and this process is very expensive.

⁵⁸The area required in an ASIC to implement a pipeline for each pixel would be unacceptably large. Therefore another approach is used for the pipeline which benefits from the very low occupancies in the pixels. A data driven pipeline is used so that when a pixel is above threshold for a given bunch crossing, a ‘time stamp’ for that pixel address is written in memory. When a first level trigger is received, the data

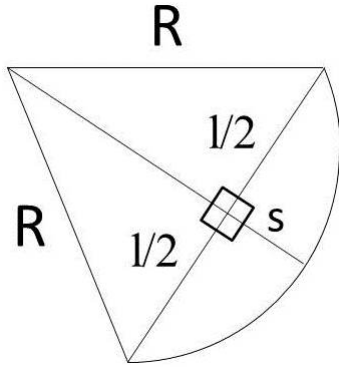


Fig. 4.22 Definition of the track sagitta s .

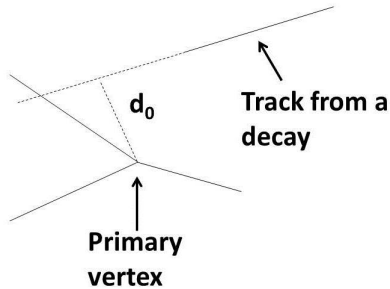


Fig. 4.23 Schematic view of tracks in the transverse plane showing tracks from the primary vertex and the definition of impact parameter from the one track resulting from a decay.

detector of the same dimensions. Therefore LHC detector systems are a compromise, in which pixels are used close to the beam pipe and strips are used at larger distances from the beam pipe.

4.6.3 Tracker Performance

Consider the track of a charged particle with momentum p (measured in GeV) perpendicular to a magnetic field \mathbf{B} . The radius of curvature R is related to the momentum by $p = 0.3BqR$. We assume that the track is measured over a length l (see fig. 4.22). From the geometry we can relate R to the ‘sagitta’ s and l by Pythagoras’s theorem $R^2 = (R-s)^2 + (l/2)^2$. For high-momentum tracks, we can neglect the s^2 term and find $1/R = 8s/l^2$. Therefore the error on $1/R$ is given by $\sigma(1/R) = 8\delta s/l^2$. In order to make approximate estimates of the momentum resolution, we will assume that the track is measured very precisely at the start and end of the trajectory but with an error given by δs at the mid-point. In this approximation

$$\sigma(1/p) = \frac{8\delta s}{0.3Bl^2}. \quad (4.41)$$

Although eqn 4.41 is a rough approximation, some general features are valid:

- (1) **B field.** The resolution improves with the value of \mathbf{B} , so we wish to use the largest value possible. Using superconducting magnets, fields up to 4T have been achieved.
- (2) **Length.** The resolution improves as l^2 , however for a tracker in a collider detector, the value of l is set by the inner radius of the electromagnetic calorimeter. Increasing l too far is therefore impractical for cost reasons. For muon spectrometers, the constraints are weaker and large values of l can be used (e.g. in the ATLAS muon spectrometer $l \sim 5$ m).
- (3) **Scaling.** The resolution is constant in $1/p$ which implies that the momentum resolution, degrades with increasing momentum.

If \mathbf{B} and l are fixed and we wish to measure momenta up to some value p_{max} we can use eqn 4.41 to estimate the required spatial resolution (see exercise 4.10). So far we have only considered the contribution of the precision of the measurement points. However in a real detector we have material, so the charged particles undergo multiple scattering (eqn 4.6). As the scattering angle is inversely proportional to the momentum, this causes a contribution to the error in $1/p$ which is constant. Therefore the momentum resolution of a real tracker can be parameterised by adding the effects of measurement precision and multiple scattering in quadrature:

$$\sigma(1/p) = A \oplus Bp \quad (4.42)$$

where A is the term due to multiple scattering and B is the term due to measurement resolution⁵⁹.

Another important measure of the performance of a tracking detector at a collider is how precisely the tracks can be extrapolated back to the

⁵⁹The optimisation of the overall resolution is an interesting trade-off because adding more measurements will decrease B but will add more material and therefore increase A .

primary vertex. Particles originating from decays of b or c quarks or τ leptons will travel for the order of 1 ps before decaying and hence if one extrapolates the tracks back they will miss the primary vertex. In the plane transverse to the beam direction this distance is called the impact parameter (see fig 4.23). The resolution in impact parameter depends on the intrinsic resolution of the tracker and multiple scattering. Therefore one requires a very high precision measurement as close to the beam line as possible and this is performed with silicon detectors (either strip or pixels). To minimise the multiple scattering, one needs to have a very thin (in radiation lengths) beam pipe and the best choice is beryllium⁶⁰.

⁶⁰Beryllium is very difficult to machine and hence expensive.

4.7 Detectors for particle jets

The energies of particles and ‘jets of particles’ are measured in detector systems called ‘calorimeters’. Ideally, all particles with the exception of muons and neutrinos (or still to be discovered neutrino like weakly interacting particles) should deposit all their energies in the calorimeter. As electromagnetic showers occupy much smaller volumes than hadronic showers (see sections 4.3), we require much finer segmentation for the front of the calorimeter than the back⁶¹. Therefore the design of calorimeter systems is usually split into ‘electromagnetic’ and ‘hadronic calorimeters’.

⁶¹We can not afford to instrument the entire calorimeter with the fine segmentation required to measure the electromagnetic showers.

4.7.1 Electromagnetic calorimeter

The depth of the electromagnetic calorimeter is chosen such that nearly all the energy of electromagnetic showers from electrons and photons of the interesting energy range is contained in this part of the calorimeter. This can be determined from Monte Carlo simulations such as those illustrated in fig. ?? . At LHC energies we need to measure electrons and photons with energies of several hundred GeV, therefore the electromagnetic calorimeter needs to be about $25X_0$ deep. Finer longitudinal sampling will also help separate showers induced by electrons from those by hadrons. The lateral shower size is set by the Moliere radius (see section 4.3) which for lead is $R_M = 1.8$ cm. The scale for the lateral size of hadronic showers is set by the hadronic interaction length, λ_I , and is typically an order of magnitude larger. We can therefore achieve further separation between showers induced by electrons and hadrons with fine lateral and longitudinal segmentation. There are two different types of electromagnetic calorimeters:

- ‘sandwich’ calorimeters with alternating layers of ‘active’ and ‘passive’ material;
- homogeneous calorimeters in which one material fulfills the function of absorber as well as actively detecting the presence of the shower.

There are many trade-offs between the choice of these approaches. In a sandwich calorimeter most of the energy is deposited in the passive

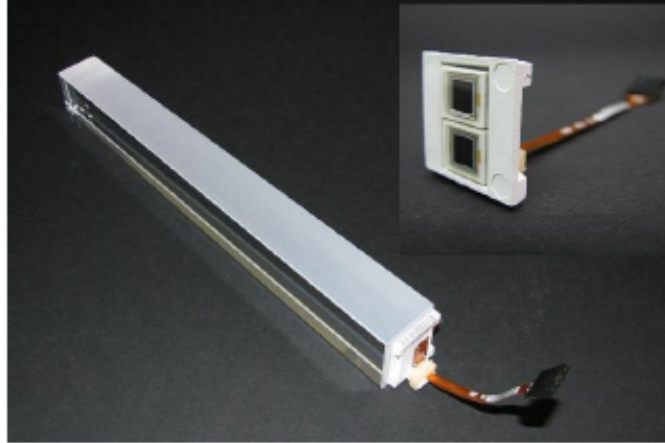


Fig. 4.24: Photograph of a PbWO_4 crystal and readout for the CMS electromagnetic calorimeter.

layers and there are significant fluctuations in the fraction of the energy deposited in the active layers. This usually limits the resolution of sandwich calorimeters and the best resolution can be achieved with homogeneous calorimeters for which this effect does not arise. However the average density of crystals used in homogeneous calorimeters tends to be lower than that of sandwich calorimeters which therefore increases the depth of the electromagnetic calorimeter. This results in larger volumes for the hadronic calorimeter and the muon system which will thus lead to an increase in cost.

4.7.2 Homogeneous Calorimeters

Homogeneous calorimeters are usually based on scintillating crystals (section 4.4.2). We will consider the CMS electromagnetic calorimeter (ECAL) as an example of this technique. At the LHC the scintillation must be fast because of the short time between bunch crossings (25 ns). The crystals must have very good radiation tolerance in order to survive many years of LHC operation. Finally the crystals must have a very high density in order to keep the dimensions small enough. The CMS EM calorimeter is based on PbWO_4 crystals with a density of 8.28 g cm^{-3} and a radiation length of 0.89 cm. About 80% of the scintillation light is emitted in less than 25 ns [?]. One challenge with this system is that the transparency of the crystals decrease with radiation and therefore sophisticated monitoring techniques are required to compensate for these effects. In addition the light output is very sensitive to temperature, so the temperature needs to be maintained at a constant value. As photomultipliers cannot be used in the very strong magnetic field, the scintillation light is readout by Avalanche Photo Diodes (APD)⁶². A photograph of one such crystal with the APD readout is shown in fig. 4.24.

⁶²In the end cap calorimeter the radiation levels are too large for the use of APDs and vacuum photo-triodes are used instead.

4.7.3 Sandwich Calorimeters

In a ‘sandwich’ calorimeter, there are alternating layers of ‘active’ and ‘passive’ material. The passive material should have high Z (to enable a relatively compact design) and lead is a common choice. The total energy detected in the active layers is only a fraction of the total energy deposited. This fraction can be measured in prototypes or small parts of the calorimeter in dedicated test beams in which the energy of the incident electrons is fixed⁶³. Before the LHC, the most common design of electromagnetic sandwich calorimeter used plastic scintillators for the active layers. The scintillation light (see section 4.4.2) needs to be guided to the photomultipliers at the back of the calorimeter. This is done using ‘wavelength shifting’ plates (see fig. 4.25). These contain fluors to shift the wavelength to longer wavelengths (typically in the green) for which the plastic is more transparent. There are several limitations with this technique:

- **Cracks.** Each tower requires a support structure to hold it in place which introduces dead zones between cells (called ‘cracks’);
- **Non-uniformity.** The absorption length for the scintillation light is typically the same magnitude as the lateral dimensions of the cell, therefore the response will depend on the impact point of the electron;
- **Radiation damage.** The scintillator will suffer significant radiation damage and very good calibration schemes are essential to track this. The most common method used is to move a radioactive source such as ^{60}Co over the calorimeter.

A newer approach to scintillator sandwich calorimeters uses wavelength shifting fibres embedded in the scintillator to transport the light to the photodetectors. This avoids the need for bulky waveguides which add to the ‘cracks’ between calorimeter cells.

In order to overcome these limitations ATLAS have developed a novel type of electromagnetic calorimeter. The calorimeter is based on a new geometry for lead absorbers and liquid argon ionization chambers. The signals are generated by electrons created by ionization, drifting in a large electric field and generating an induced current at the electrodes (see section 4.4)⁶⁴. The fundamental problem with this technique for use at the LHC is that the typical drift times for the electrons is ~ 400 ns which is much longer than the time between bunch crossings of 25 ns. The solution is based on very fast ‘bi-polar’ pulse shaping electronics, in which most of the signal is not detected but a suitably fast pulse is generated. This is illustrated in fig. 4.26. As most of the signal is not utilized, it is essential to lower the noise in order to maintain the signal to noise ratio. This is achieved by lowering the capacitance and inductance of the electrodes using a novel ‘accordion’ geometry⁶⁵. as shown in fig. 4.27. An important advantage of this technique is that liquid argon is inherently radiation hard. It is relatively easy to divide the readout cells to the desired lateral and longitudinal granularity. Another critical

⁶³At the LHC the rate of Z production is so high that ‘in-situ’ calibration can be performed.

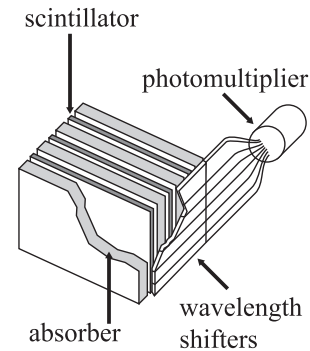


Fig. 4.25 Schematic view of one cell of a sandwich scintillator calorimeter with wavelength-shifting plates to guide the light to the photomultiplier at the back.

⁶⁴This is very similar to a wire chamber operating in the ‘ionization chamber’ region, in which there is no gas gain. However as a liquid is very much denser than a gas, a high energy charged particle can create sufficient ionization for the signal to be detectable.

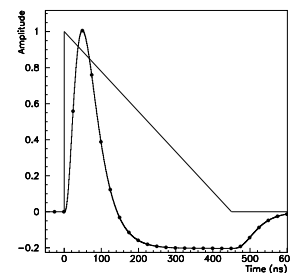


Fig. 4.26 Signal pulse shape in the ATLAS liquid Argon calorimeter. The triangular shape is the current pulse created by the drift of the electrons. The curve shows the pulse shape after shaping with a bi-polar pulse shaper.

⁶⁵This design was invented by a French

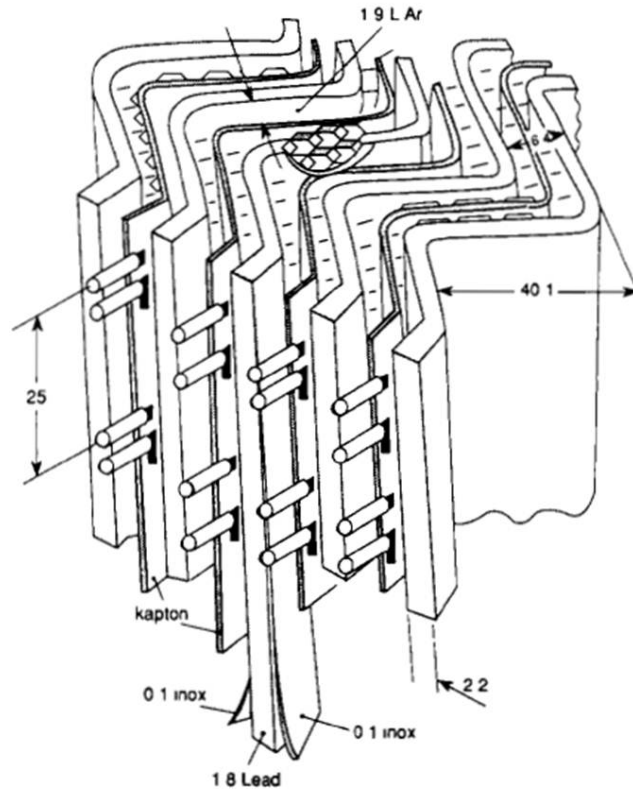


Fig. 4.27: Sketch of a small section of a prototype for the ATLAS electromagnetic calorimeter, illustrating the ‘accordion’ structure. The absorber plates are made from lead lined with stainless steel. The liquid argon is contained between the absorber plates and the copper/kapton electrodes are attached to the absorber plates. All dimensions are in mm.

advantage is that the structure is self supporting so there is no need for passive material between cells, thus avoiding the cracks inherent in calorimeters based on plastic scintillators for the active layers.

4.7.4 Resolution

The energy resolution of a typical electromagnetic calorimeter can be parametrized as

$$\frac{\Delta E}{E} = \frac{a}{\sqrt{E}} \oplus b/E \oplus c \quad (4.43)$$

where a , b and c are constants and the different terms are added in quadrature. The constant a represents the ‘stochastic term’, b represents the contribution from electronic noise and c is a constant term. In a calorimeter using scintillator, if at a given energy the mean number of detected photons is N , there will be Poisson fluctuations giving a contribution to the stochastic term

$$\frac{\Delta E}{E} \sim \frac{\Delta N}{N} \sim \frac{\sqrt{N}}{N} = \frac{1}{\sqrt{N}} \Rightarrow \frac{\Delta E}{E} = \frac{a}{\sqrt{E}}$$

Table 4.2: Electromagnetic calorimeter resolution for prototype calorimeters measured in test beams.

experiment	ATLAS	CMS
a % $(GeV)^{0.5}$	10.0	2.8
b (GeV)	0.4	0.12
c (%)	-	0.3

However in a sandwich calorimeter this effect is usually negligible compared to the ‘sampling’ fluctuations, i.e. the fraction of energy deposited in the active layers.⁶⁶ The constant b represents the contributions from electronic noise and should be negligible at high energies. The constant term c represents the effects of residual non-uniformities in response across the cell and over all cells as well as variations in time. With the aid of good calibration procedures the constant term can be reduced to below 1%⁶⁷. Measured parameters from test beam studies for the ATLAS [?] and CMS [?] electromagnetic calorimeters are given in Table 4.2. However during LHC operation, there are other factors which will degrade the resolution, such as radiation damage, uncertainties in the calibration constants and ‘pile-up’ backgrounds (particles from extra collisions in the same bunch crossing). For the very important Higgs decay, $H \rightarrow \gamma\gamma$, the precision of the angular measurement also contributes to the mass resolution. These factors favour the higher granularity segmentation possible and the intrinsic stability and radiation hardness of liquid argon compared to a scintillator calorimeter. The result is that the mass resolution for the Higgs decay $H \rightarrow \gamma\gamma$, is comparable for ATLAS and CMS.

4.7.5 Hadronic calorimeter

The hadronic calorimeter surrounds the electromagnetic calorimeter. Ideally the combined electromagnetic and hadronic calorimeter should contain nearly all the energy from showers from hadrons entering the calorimeter (mostly π^\pm). An indication of the required depth of the calorimeter can be deduced from the curves in fig. 4.8. The practical depths for hadronic calorimeters are constrained by cost and available space but a rule of thumb is that at LHC energies a depth of at least about 10 nuclear interaction lengths is required. Therefore homogeneous hadronic calorimeters would be too large so are not a practical option and hadronic calorimeters will be of the ‘sandwich’ type. The resolution for hadronic calorimeters is greatly reduced if the calorimeter is not ‘compensating’, which means that the ratio of the response to electrons to that of hadrons, e/h is significantly different from unity (see section 4.3.6). There are several possible approaches to achieving compensation in hadronic calorimeters:

⁶⁶There are many interesting trade-offs here. If the fraction of scintillator over passive material is increased the sampling fluctuations are reduced but the size and hence the cost of the calorimeter will increase. If one tries to use thinner absorber and scintillator plates, it becomes very difficult to efficiently collect the scintillation light which will eventually degrade the resolution. There is no perfect design.

⁶⁷At the LHC, the very large sample of events from $Z \rightarrow e^+e^-$ provide very powerful samples for ‘in-situ’ calibration of the electromagnetic calorimeters.

- **Tuning absorber to active thickness ratio.** The energy loss for electrons scales as Z^2 compared to Z for charged hadrons, therefore in thicker absorbers the value of e/h can be lowered (however this has other problems that will be discussed later). Lower Z cladding can be used to absorb low energy photons preferentially, which also reduces e/h ;
- **Increasing the hadronic response.** Instead of trying to suppress the response to electrons, we can try to enhance the response to hadrons. There are many low energy neutrons which can be indirectly detected by elastic scattering off nuclei. The optimal nucleus is hydrogen so detectors containing hydrogen, such as organic scintillators can be used;
- **Use of depleted uranium** One suggestion to increase the hadronic response was to have uranium absorber plates and use the energy released by fission after fast n capture⁶⁸;
- **Software compensation.** In a finely grained calorimeter, calibration procedures can be optimised to try to achieve compensation and this approach is discussed below;
- **Dual readout.** The idea is to readout the shower energy using two different techniques with very different values for e/h . A prototype of such a hadronic calorimeter has been built by the DREAM collaboration and it uses copper tubes, each filled with scintillator and quartz fibers. The signal from the scintillator (S) and the Čerenkov (C) radiation in the quartz fibres are measured separately. The values of e/h are very different for the S and C signals which allows for the determination of the electromagnetic fraction f_{em} for individual showers. The effect of e/h being different from unity can therefore be corrected, effectively achieving the good hadronic resolution of compensating calorimeters.

⁶⁸This was the motivation for the use of uranium in the ZEUS calorimeter which achieved compensation. However the two first items were more important than fission.

⁶⁹The ATLAS barrel calorimeter has $e/h \approx 1.4$.

⁷⁰The correction factors also depend on the energy as well as the local energy density.

Although compensating calorimeters have been built, there are disadvantages in cost and/or resolution for electrons and photons and the calorimeters for the LHC experiments are not compensating⁶⁹. In a highly segmented calorimeter such as that used by ATLAS, the hadronic resolution can be improved by ‘software compensation’; the secondary electromagnetic showers are smaller than hadronic showers, so they lead to higher energy density in the calorimeter cells. Therefore the electron response can be decreased by de-weighting cells with large energy, thus making the response closer to being compensating and therefore improving the resolution. If the calorimeter cells are calibrated using electrons, the naive estimate of the energy in a hadronic shower would be given by $E = \sum_i E_i$, where E_i is the energy in the i^{th} calorimeter cell. As electromagnetic showers are more compact, the cells with higher local energy density will probably have arisen from electromagnetic showers. A correction factor is applied for hadronic showers. The correction factors decreases for showers with higher local density of energy deposition⁷⁰. The calibration procedure used to determine the calibration factors aims to reconstruct the true energy on average and to optimize the resolution.

Table 4.3: Energy resolution for prototype hadronic calorimeters measured in test beams.

experiment	ATLAS tile calorimeter	ZEUS
a % $(GeV)^{0.5}$	52	35
b (GeV)	1.6	-
c (%)	3.0	-

The resolution for hadronic calorimeters can be parameterized by the same form as for electromagnetic calorimeters (eqn 4.43). The stochastic term will be larger because of the relatively coarse sampling and if the calorimeter is non-compensating there will be a large constant term, which will dominate the resolution at high energies. If the calorimeter is not sufficiently deep, the energy lost at the back of the calorimeter will also contribute to the constant term. Any crack regions between cells or non-uniformity of the response over a cell will also add to the constant term. Typical examples of hadronic resolution for compensating and non-compensating calorimeters are given in Table 4.3. The superior resolution of the compensating ZEUS calorimeter [?] compared to the non-compensating ATLAS scintillating tile calorimeter [?] is clear but even so the resolution is far inferior to that achieved by electromagnetic calorimeters. However the compensation achieved in the ZEUS calorimeter came at the price of degrading the electromagnetic resolution. So as usual in detector physics there is no perfect answer and designs must be optimized to the requirements of a particular experiment.

4.8 Detectors for particle identification

In this section we will review some detector techniques for particle identification. Some particle identification is performed by combining signals in different types of detectors⁷¹ but here we restrict ourselves to types of detectors that give standalone particle identification.

⁷¹e.g. a high momentum track that is matched to an electromagnetic shower in a calorimeter can be identified as an electron

4.8.1 Particle identification with Čerenkov detection

There are two practical applications of Čerenkov radiation for particle identification:

- **Threshold counter.** If we measure the momentum of a charged particle, p , we can determine its speed depending on what particle type it is (and hence mass). For some range of momentum we can arrange that $v > 1/n$ for one type of particle (e.g. π^\pm) but below threshold for another (e.g. K^\pm). Therefore we can separate π^\pm from K^\pm depending on whether a Čerenkov signal was detected;

- **Ring Imaging Čerenkov (RICH).** A RICH represents a more sophisticated use of Čerenkov radiation in which we measure the direction of Čerenkov photons. This requires optics to focus the photons of a given angle to a particular location on the photon detector. We then associate particular Čerenkov photons with particular charged particles and fit a ring (hence the name of the technique) and measure the Čerenkov angle. If we know the refractive index of the medium we can then determine the speed of the charged particle. Knowing the momentum, p from an independent detector then allows us to estimate the mass of the charged particle and hence identify it as a pion, Kaon etc We will look at an example RICH detector in chapter 10.

4.8.2 Particle identification with transition radiation

We have seen that charged particles crossing a boundary between two dielectric layers can emit X-rays. As the transition radiation increases with the Lorentz γ factor, for practical purposes the yield is only significant for high energy electrons, which therefore provides a method to separate high energy electrons from charged hadrons. As the photon yield per dielectric boundary is so low, we need many such boundaries. This sets a lower limit on the required length for a useful transition radiation detector.⁷² The transition radiation photons are in the X-ray region. These X-ray photons can be detected in wire chambers with a large fraction of a heavy noble gas like xenon. (for xenon, $Z=54$, which results in a large absorption cross section for X-rays, thus increasing the probability of X-ray absorption in a thin layer of gas). The energy deposited by X-rays is larger than the typical energy deposited by ionization in the gas, so a suitable discriminator level can be set which is sensitive to the X-rays from transition radiation but is rather insensitive to ionization⁷³.

⁷²This is not a problem for fixed target experiments, however this is very problematic for collider detectors for which the radial space for the tracker is limited by the inner radius of the calorimeter.

⁷³The problem is that there are large statistical fluctuations in the magnitude of the energy loss deposited by ionization in a short path length in a gas.

4.8.3 Particle identification with Ionization

We saw that the rate of energy loss by ionization depends on the speed (β) of the particle (see eqn. 4.5). Therefore if we can make a suitable precise measurement of the energy loss by ionization and the momentum of a particle, we can achieve some separation between particles with different masses (e.g. pions and kaons). The momentum can be measured by a tracking detector in a magnetic spectrometer and the amplitude of the signals in the elements of the tracking detector provide a measurement of the energy loss by ionization. The first difficulty with this technique is the very large fluctuations in energy loss by ionization in thin layers, so if a wire chamber is used a very large number of samples is required to achieve useful particle identification. The second problem is that the rate of energy loss as a function of momentum ‘plateaus’ at high momentum, so this technique is only useful at lower energies.

4.9 Magnetic fields

We need magnetic fields for trackers and muon spectrometers in order to use the measured trajectory to reconstruct the momenta. The magnets are usually based on the same NiTi superconducting technology discussed for accelerators in section 3.2.1. The volumes of the magnets are very much larger and although the magnetic fields are smaller, the energy stored in the magnetic fields are very much larger, which generates new engineering challenges.

4.9.1 Magnetic fields for trackers

The usual choice of field configuration for trackers at colliders is a solenoid (with the axis along the beam line). In order to minimize the volume and the cost, one option is to place the solenoid between the tracker and the calorimeter. Clearly too much ‘passive’ material upstream of the calorimeter will degrade the resolution of the electromagnetic calorimeter. Therefore the fields are generated using superconducting magnet, with field strengths up to 2T being typical. The CMS magnet has a field strength of 4T and has a larger radius so that the entire calorimeter system is housed inside the solenoid.

4.9.2 Magnetic fields for muon spectrometers

One option for the magnetic field for the muon spectrometer is to use magnetized iron. If there is a superconducting solenoid for the tracker, the magnetic flux will return from the solenoid through the iron surrounding the solenoid. In this case the iron serves multiple purposes: it can be the passive absorber for the hadron calorimeter and act as shielding to remove particles other than muons before they reach the muon chambers as well as acting as the return ‘yoke’ for the solenoid. The iron is instrumented with tracking chambers (using a variety of wire chambers) and the reconstructed muon tracks in these chambers can therefore be used to determine the momenta. The momentum resolution for these tracks is limited by multiple scattering to about 10%. In the CMS approach the muon spectrometer tracks are linked to the much more precisely measured tracks in the tracker and hence a good muon momentum resolution can be achieved⁷⁴.

In the approach used for ATLAS, the magnetic field for the muon spectrometer is generated by 8 large superconducting toroids in the central (‘barrel’) region and 8 smaller superconducting coils in each end cap. (see fig. 4.28). The average magnetic field in the tracking volume is in the range $\sim 0.5 - 1\text{T}$ but very good resolution is achieved by tracking over a long length $l \sim 5\text{m}$.⁷⁵ Since most of the volume is air the momentum resolution is not so limited by multiple scattering as for magnetized iron. Another advantage of this field configuration is that it allows for reconstruction of precise muon momenta independently of the tracker⁷⁶.

⁷⁴See exercise 4.9 for a discussion of some issues associated with muon triggers for this configuration.

⁷⁵The total energy stored in the ATLAS magnetic fields is about 1.6 GJ, which is the same magnitude as the kinetic energy in a TGV train with a mass of 385 t traveling at 330 km/hr.

⁷⁶The most precise muon measurement is then obtained by combining the estimates from the tracker and the muon spectrometer.

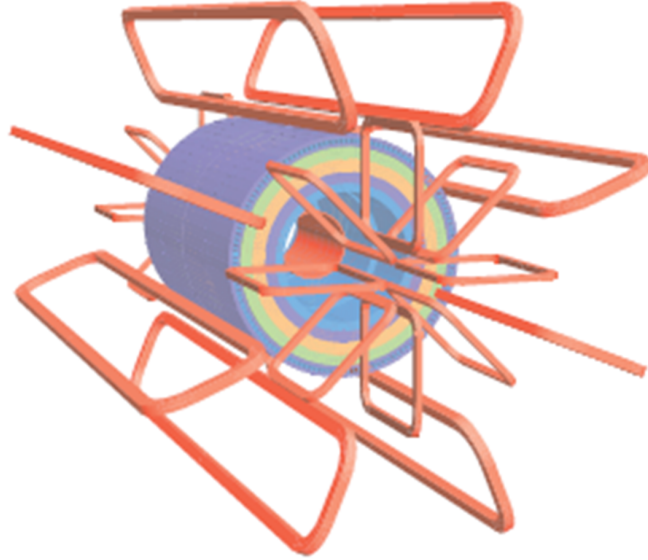


Fig. 4.28: Schematic view of the ATLAS toroid coils. The eight barrel toroid coils with the interleaved end-cap coils are shown. The cylinder shows the return flux for the solenoid. The length is 25.1 m and the outer diameter is 20.1 m.

4.10 Trigger

The trigger is an electronic and software system operating in ‘real’ time to reduce the raw data rate to that which can be permanently stored. The trigger should keep as much of the interesting physics while rejecting the maximal amount of background events. The aim is to bring the rate down from the raw interaction rate to the maximum at which data can be stored on permanent storage, whilst keeping as large a fraction of the signal events as possible. Traditionally this rate was typically of the order of a Hz but advances in computer technology now allow for far higher rates. The event rates are very different for different colliders. At e^+e^- colliders, the rates are relatively low ($O(\text{Hz})$) but the rates at hadron colliders have been increasing. At the LHC there are multiple interactions per bunch crossing (50 ns in 2012 running and 25 ns for the nominal LHC operation) and the trigger reduces this rate to a level of $O(500 \text{ Hz})$.

Typically there are three trigger stages or levels. In older generation of experiments, at the first, fastest level, the selection is based on the timing and the signal level of detector components. The implementation is usually in fast hardware logic operations on outputs from units like comparators and coincidence units. Detector signals are required to be in coincidence with colliding beam bunches and be compatible with tracks and energy deposits of particles coming from a small region where colliding beam bunches overlap. More sophisticated algorithms are required for the LHC (see section 4.10.1). At the second level, fast processors are used to reject background events, like those coming from cosmic rays or stray accelerator particles in a halo around the beam pipe or from beam

particles interacting with molecules and atoms in a residue gas in the beam pipe. At this level we also need to reject genuine physics events produced by colliding beam particles which are not interesting. The third level is often comparable to the off-line reconstruction. Farms of computers select signal events to be stored for off-line reconstruction and analysis. The main difference between the third level trigger programs and off-line programs is in use of calibration constants and correction procedures which need to be obtained or developed separately off-line.

4.10.1 LHC triggers

The issue of efficiently triggering on interesting physics events, while maintaining a manageable readout rate is one of the main challenges for LHC detectors. At design luminosity the rate of pp collisions is about 1 GHz and this rate has to be reduced to $O(500 \text{ Hz})$ for data to be stored for subsequent offline analysis. The first level trigger (L1) uses signals from the full detector, which given the finite speed of light makes it impossible to generate a trigger decision from one bunch crossing before the following bunch crossing occurs (25 ns at nominal LHC operation). This apparently insoluble problem is solved with the aid of a ‘pipelined’ system.⁷⁷ The data is stored on detector in ‘pipeline’ memory (see sec. 51) while the L1 decision is being made by a custom pipeline hardware processor. In such a pipelined processor, one step of the trigger process operates on the data for a particular event in one clock cycle and then the next step is operated in the following clock cycle. The number of allowed steps for such a processor, depends on the depth of the pipeline memory in which the data is stored⁷⁸. As all bunch crossings have genuine pp collisions, it is no longer sufficient to simply reject non-beam backgrounds; the L1 trigger must decide which real events to keep. The L1 trigger uses interesting signatures like high transverse momentum electrons by performing hardware sums of the energy deposited in neighbouring cells in the electromagnetic calorimeter. A global L1 trigger decision is made on the basis of several signatures (e.g. high transverse momentum muon candidates, large missing transverse energy etc.). This L1 trigger typically reduces the rate to $O(100 \text{ kHz})$. At this rate it is now feasible to read out all the data corresponding to triggered bunch crossings

⁷⁹. At this stage the data can be processed by very large computer farms, which use the full detector granularity to reduce the rate to the required $O(500 \text{ Hz})$.

⁷⁷This approach was pioneered by the H1 and ZEUS experiments at DESY.

⁷⁸A typical pipeline depth of 132 corresponds to a time of $3.2 \mu\text{s}$, which is sufficient to allow for the signals to reach the trigger processor, for a trigger decision to be made and for that decision to be fed back to the electronics on the detector.

⁷⁹The read out is performed using optical fibre links

4.11 Detector systems

Now that we have seen the principles behind the design of detector subsystems, we can start to understand how these principle are applied in the designs of real detectors. We will first look at collider detectors and then briefly consider neutrino detectors. A case study of a dark matter detector will be given in chapter 13.

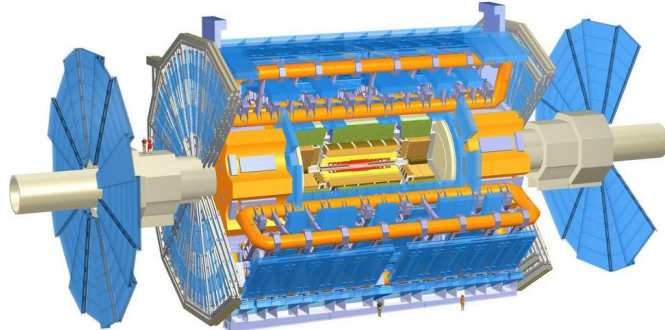


Fig. 4.29: Schematic view of the ATLAS detector.

4.11.1 Collider detectors

⁸⁰We will consider some unique aspects of the LHCb detector in chapter 10.

We will take the ATLAS and CMS detectors as examples of collider detectors⁸⁰. The ATLAS detector is illustrated schematically in fig. 4.29. The tracker is immersed in a 2T magnetic field and consists of silicon detectors closest to the beam line and a Transition Radiation Tracker (TRT) at larger radius. The silicon detector contains three layers of pixels closest to the beam pipe to provide the best resolution for the impact parameter and layers of silicon strips at larger radius. The TRT is made from cylindrical ‘straw’ tubes, with each tube working as an independent cylindrical drift chamber. The tubes are interleaved with mylar foils to generate transition radiation to enhance electron identification. The electromagnetic calorimeter is based on the liquid argon accordion calorimeter (see section 4.7.3). In the central region the hadronic calorimeter uses an iron-scintillator sandwich design. The light from the scintillators is coupled to the photomultipliers using wavelength shifting fibres. The novel feature of this design is that the steel absorber plates are rotated by 90° compared to the conventional design in which the plates are perpendicular to the direction of incidence of primary particles. This has the advantage that the calorimeter cells are self-supporting thus avoiding ‘dead’ material between cells. Although the calorimeter system is not compensating, the fine granularity allows for the use of software compensation to improve the resolution. Calorimeters extend up to pseudorapidity $\eta \approx 5$ in order to reconstruct missing transverse momentum (see chapter 8). The muon spectrometer uses the toroidal coils discussed in section 4.9.2. In the central barrel region, the muon tracks are measured using detectors based on drift tubes. However the signals are too slow to participate in the first level trigger (see section 4.10) and therefore faster but lower resolution detectors are also used.

A ‘slice’ of the CMS detector is shown in fig. 4.30 and the response to different types of particles is illustrated schematically. There is a very large all-silicon tracker consisting of three layers of pixel detector and 10 layers of strip detectors immersed in the 4T solenoidal magnetic field, which provides very good momentum resolution for charged par-

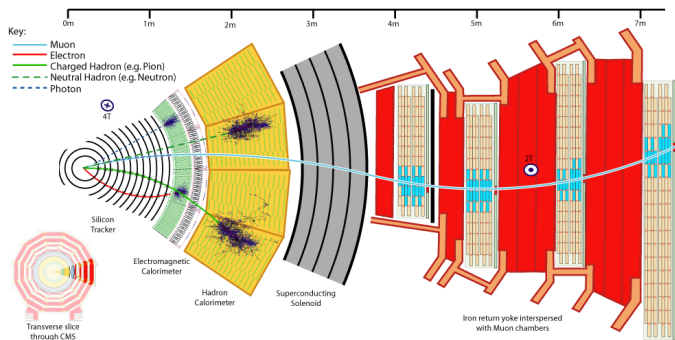


Fig. 4.30: Schematic view a slice of the CMS detector in the plane transverse to the beam axis.

ticles. The electromagnetic calorimeter uses PbWO_4 crystals (see section 4.7.2). The hadronic calorimeter uses a brass/scintillator sandwich calorimeter. As with ATLAS, forward calorimeters extend the coverage to close to the beam pipe. The muon chambers are interleaved with the return yoke of the solenoid. The muon chambers are used for the first level muon trigger, but the high precision measurement of the muon momenta is made in the tracker.

4.11.2 Neutrino detectors

The optimization of neutrino detectors is very different to that of collider detectors because the very small cross sections imply the need for very massive detectors in order to obtain useful event rates⁸¹. Given the sizes involved, we are obliged to use cheaper detector technologies than at hadron colliders. The requirements depend on the neutrino energies. For an accelerator neutrino experiment, a typical requirement is to have a very large target mass and be able to measure:

- **Electrons.** We need to measure electrons from neutral current scattering (see chapter ??) off electrons $\nu_x e^- \rightarrow \nu_x e^-$ (where ν_x is any flavour of neutrino, or from similar processes with scattering on the nuclei;
- **Muons.** We have muons from charged current interactions $\nu_\mu N \rightarrow \mu^- N'$ where $N(N')$ are the target (scattered) nucleus and X represents any hadrons produced in the interaction;
- **Hadrons.** For the neutral current interactions off nuclei the only particles we can measure are the outgoing hadrons. Measurements of produced hadrons also improve the determination of the event kinematics for charged current interactions.

In general we can use calorimeters to measure electrons and hadrons. If the passive absorber plates are made from magnetised iron and we instrument the gaps between absorbers with some tracking detector we can determine the tracks caused by muons. We can then identify muons as particles that penetrate deeper into the detector than hadrons and at the same time we can estimate the momentum by measuring the

⁸¹This is particularly true for neutrino detectors in laboratory oscillation experiments in which we need a detector far from the neutrino source in order to study oscillations (see chapter ??).

curvature of the tracks. We will see how these principles are applied in practice in the MINOS far detector in chapter 11.

Chapter summary

- The physics of interactions of high energy particles in matter has been reviewed.
- The basic detector physics of how a signal is generated by charged particles was explained.
- A brief summary of how different types of scintillators work has been given.
- The basic concepts of trigger systems are explained.
- Different detector systems are discussed and how to combine them into a general purpose detector.
- More case studies of real particle physics detectors are given in other chapters.

Further reading

J. Beringer et al. (Particle Data Group), *Particle detectors*, Phys. Rev. D86, 010001 (2012). The review article 'passage of particles through matter' gives a thorough discussion. The review article on 'particle detectors at accelerators' gives a more advanced and thorough discussion than given in this chapter.

Dan Green (Ed) *At the Leading Edge The ATLAS and CMS LHC experiments*, World Scientific Publishing 2010. A collection of advanced review articles on different aspects of the detectors.

Claus Grupen and Boris Shwartz, *Particle Detectors*, Second Edition, Cambridge University Press, 2008. A

very comprehensive description of many detector technologies.

Konrad Kleinknecht, *Detectors for Particle Radiation*, Second Edition, Cambridge University Press, 1998. A short and clear introduction to detector physics.

Walter Blum, Werner Riegler and Luigi Rolandi, *Particle Detection with Drift Chambers*, Second Edition, Springer 2008. The definitive advanced textbook on this subject
H. Spieler, *Semiconductor Detector Systems*, Oxford University Press, 2005. A very good advanced textbook on silicon detectors and the associated electronics.

Exercises

- (4.1) Starting from eqn 9.12 and using a change of variable, derive eqn 4.1.
- (4.2) Consider elastic scattering of a heavy particle mass M with speed β on a stationary electron.
- (a) Let the kinetic energy of the scattered electron be T in the frame in which the electron was initially at rest. Show that the 4-momentum transfer evaluated in this frame is $Q^2 = 2m_e T$.
- (b) Assuming $m/M \ll 1$ and $\gamma m/M \ll 1$ show that the maximum kinetic energy of the electron after the scattering in the lab frame is $T_{max} = 2\gamma^2 \beta^2 m_e$. Hint: consider the problem in the CMS and then use a Lorentz transformation from the CMS to the lab.
- (4.3) Calculate the Fourier coefficients for a 'top-hat' function defined by $f(x) = 1$ for $0 < x < a$ and 0 elsewhere. Use this result to derive eqn 4.17 starting from eqn 4.16.
- (4.4) (a) A very crude model of the initial development of an electromagnetic shower is that a high energy electron or positron of energy E_0 undergoes a bremsstrahlung process after a distance L (one radiation length) and loses half of its energy to a secondary photon, or that a high energy photon initiates a pair production process after travelling a distance L , splitting its energy equally between the two secondary particles. These processes continue until the photons and charged particles each have an energy less than the critical energy $E_C (\ll E_0)$, at which point the multiplication ceases. Develop this model and answer the following questions for both an incident electron of energy E_0 and for an incident photon of the same energy.
- (i) How many photons plus charged particles will there be after N radiation lengths?
- (ii) What is the energy of each particle in the shower after N radiation lengths?
- (iii) What is the depth (in units of L) at which the number of particles in the shower is a maximum, and what is the number of particles at maximum?
- (b) Compute the depth and the number of particles when multiplication ceases for a 4 GeV electron entering lead glass ($L = 2.5$ cm, $E_C = 10$ MeV). (c) Explaining any assumptions you make, how would the resolution of an electromagnetic calorimeter scale with the energy of the incident electron, E ?
- (4.5) Calculate the direction of Čerenkov radiation with respect to the direction of motion of fast charged particles in water. The refractive index of water is 1.33.
- (4.6) Calculate the threshold energy above which electrons and muons emit Čerenko radiation. What consequences does this have for the measurement of
- (a) the solar neutrino flux?
- (b) the flavour ratio of atmospheric neutrinos?
- (4.7) A very simple model of a high-precision silicon 'micro-vertex detector' (MVD) consists of two concentric cylindrical layers surrounding the beam-line. The first layer is at radius of $R_0 = 5$ cm, and the separation between the first and second layer is $L = 2$ cm. The intrinsic measurement resolution of a hit is $\sigma = 10 \mu\text{m}$ in the $R\phi$ direction (roughly orthogonal to the trajectory of a particle with large transverse momentum).
- Show that (neglecting multiple scattering) the uncertainty on the impact parameter (distance of closest approach to the beam line in the plane perpendicular to the beam), σ_a , is given by
- $$\sigma_a = \frac{\sigma}{L} \sqrt{(R_0 + L)^2 + R_0^2},$$
- and calculate it for the parameter values given above. How does σ_a change if (i) L is doubled; (ii) R_0 is increased to 8 cm? What factors limit the ability to decrease R or increase L . Assume each layer has a thickness of 2% of a radiation length. How does multiple scattering affect the impact parameter resolution? For what momentum would the uncertainty in the impact parameter from measurement error be equal to that from multiple scattering?
- (4.8) Consider a cylindrical detector immersed in a uniform solenoidal magnetic field B . Let R be the radius of curvature of a track in the plane transverse to the beam line (measured in metres). Show that the transverse momentum $p_T = 0.3BR$. A very simplified model for the resolution of a tracker assumes that the track is precisely located at the start and end of the trajectory but there is a measurement error in the transverse plane of σ_s at a radius

- of half the outer radius of the tracker ($L/2$). Using this model determine the transverse momentum resolution as a function of p_T . For such a detector with $B = 4T, L = 1\text{ m}$ and $\sigma_s = 10\ \mu\text{m}$, estimate the largest value of p_T that could be measured with an error less than $1/3$ of the value.
- (4.9) Consider a solenoid providing a uniform magnetic field $\mathbf{B} = B_1\hat{z}$ for a radius $0 < R < R_1$. All the flux returns through a return yoke such that $\mathbf{B} = B_2\hat{z}$ for a radius $R_1 < R < R_2$. (a) Show that $\int_0^{R_2} B(r)dr = 0$. (b) What is the force on a charged particle moving with a velocity v in the xy plane? Hence find the torque on the charged particle. (c) Now consider the trajectory of a muon created on the axis of the solenoid ($r = 0$). Combining the results of (a) and (b) show that there is no net change in angular momentum of the muon during its trajectory from $r = 0$ to $r = R_2$. Explain why this means that the trajectory of the muon after it exits the return yoke (ie at $r = R_2$) points back to the axis (d) These calculations have ignored multiple scattering, how would this change the result qualitatively? (e) Discuss the implications for the measurement of muon momenta in this geometry.
- (4.10) We wish to measure a charged particle with momentum transverse to the beam line of $p_T = 500\ \text{GeV}$ in a tracking detector immersed in a solenoidal field of $\mathbf{B} = 2\ \text{T}$. If we require a momentum resolution $\sigma(1/p_T)/(1/p_T) = 0.3$ estimate the spatial resolution required for the sagitta measurement. Discuss which detector technology would be appropriate.
- (4.11) Consider a cylindrical drift chamber with a radius of $4\ \text{mm}$, operated at a voltage of $2\ \text{kV}$. If the positive ions have a mobility of $1\ \mu = 1\text{cm}^2\text{V}^{-1}\text{s}^{-1}$ calculate the maximum drift time. How long does it take to accumulate 50% of the full signal?
- (4.12) Consider a MWPC with anode spacing of d . Consider the coordinate x in the plane of anode wires. Calculate the RMS in the difference in x between the location of a track and the nearest wire, hence justify the claim that the resolution is $d/\sqrt{12}$.
- (4.13) Consider a silicon microstrip detector(see fig. 4.19) with resistivity of the silicon of $\rho = 10\text{k}\Omega\ \text{cm}$ and a thickness of $w = 300\ \mu\text{m}$. Determine the bias voltage required to fully deplete the detector ($V_{\text{depletion}}$). If an electron-hole pair is created at a distance x from the p -type electrode, calculate the drift time of the hole in terms of the mobility of the holes μ_h . For silicon, $\mu_h = 480\ \text{V/cm}$, determine the charge collection times for holes created at depths $x = 0.5w$ and $x = 0.9w$. If the detector was operated at a bias voltage $V = 2V_{\text{depletion}}$, how would the charge collection times change? Hence discuss the advantages of operating the detector at a voltage greater than the depletion voltage. What limits the detector voltage that can be applied in practice?
- (4.14) The leakage current in a silicon detector is a source of noise. If the leakage current in one channel is I_{leak} and the signal is integrated over a time T , make a simple estimate of N_{leak} , the contribution of the leakage current to the noise. For a typical LHC silicon detector $T \sim 25\ \text{ns}$ (the bunch spacing). Estimate N_{leak} for two cases: (a) $I_{\text{leak}} = 1\ \text{nA}$ (typical for an unirradiated strip detector) and (b) $I_{\text{leak}} = 1\ \mu\text{A}$ (typical for a heavily irradiated strip detector). Compare this noise values with the signal expected from a $300\ \mu\text{m}$ thick silicon detector. Design a simple filter circuit to minimise the leakage current noise while keeping as much as possible of the signal. Suggest suitable values for components of your filter for an LHC microstrip detector.
- (4.15) Consider a silicon microstrip detector with n -doped implants (strips) in p -doped bulk silicon (see fig. 4.19). Make a rough sketch of the ‘weighting’ field (see section 4.4.1) in the region around one strip and indicate on it the region in which the weighting field will be large. A charged particle crosses such a detector in a direction perpendicular to the plane of the silicon and creates electron-hole pairs uniformly along its trajectory. For a reverse biased detector, which way will the electrons (holes) drift? By combining the above considerations, show that the resulting signal will be dominated by the motion of holes, rather than electrons.